Seasonal-to-Decadal Variability and Prediction of the Kuroshio Extension in the GFDL Coupled Ensemble Reanalysis and Forecasting System

YOUNGJI JOH,[a,b] THOMAS L. DELWORTH,[b] ANDREW T. WITTENBERG,[b] WILLIAM F. COOKE,[b] XIAOSONG YANG,[b] FANRONG ZENG,[b] LIWEI JIA,[b] FEIYU LU,[a,b] NATHANIEL JOHNSON,[b] SARAH B. KAPNICK,[b] ANTHONY ROSATI,[b,c] LIPING ZHANG,[b,c] AND COLLEEN MCHUGH[b,d]

[a] *Atmospheric and Oceanic Sciences Program, Princeton University, Princeton, New Jersey*
[b] *Geophysical Fluid Dynamics Laboratory/NOAA, Princeton, New Jersey*
[c] *University Corporation for Atmospheric Research, Boulder, Colorado*
[d] *Science Applications International Corporation, Reston, Virginia*

(Manuscript received 21 June 2021, in final form 1 February 2022)

ABSTRACT: The Kuroshio Extension (KE), an eastward-flowing jet located in the Pacific western boundary current system, exhibits prominent seasonal-to-decadal variability, which is crucial for understanding climate variations in the northern midlatitudes. We explore the representation and prediction skill for the KE in the GFDL SPEAR (Seamless System for Prediction and Earth System Research) coupled model. Two different approaches are used to generate coupled reanalyses and forecasts: 1) restoring the coupled model's SST and atmospheric variables toward existing reanalyses, or 2) assimilating SST and subsurface observations into the coupled model without atmospheric assimilation. Both systems use an ocean model with 1° resolution and capture the largest sea surface height (SSH) variability over the KE region. Assimilating subsurface observations appears to be essential to reproduce the narrow front and related oceanic variability of the KE jet in the coupled reanalysis. We demonstrate skillful retrospective predictions of KE SSH variability in monthly (up to 1 year) and annual-mean (up to 5 years) KE forecasts in the seasonal and decadal prediction systems, respectively. The prediction skill varies seasonally, peaking for forecasts initialized in January and verifying in September due to the winter intensification of North Pacific atmospheric forcing. We show that strong large-scale atmospheric anomalies generate deterministic oceanic forcing (i.e., Rossby waves), leading to skillful long-lead KE forecasts. These atmospheric anomalies also drive Ekman convergence and divergence, which forms ocean memory, by sequestering thermal anomalies deep into the winter mixed layer that re-emerge in the subsequent autumn. The SPEAR forecasts capture the recent negative-to-positive transition of the KE phase in 2017, projecting a continued positive phase through 2022.

KEYWORDS: Atmosphere-ocean interaction; Boundary currents; Climate prediction; Forecasting; Seasonal forecasting; Climate models; Coupled models; Ensembles; Reanalysis data; Climate variability; Decadal variability; Oceanic variability

1. Introduction

The Kuroshio Extension (KE) is an eastward extension jet of the poleward-flowing, warm ocean current, the Kuroshio, on the west side of the North Pacific Ocean. Over the KE region, sea surface height (SSH) and oceanic heat content anomalies exhibit strong variability on interannual and longer time scales (Qiu 2002). The KE is well known as a turbulent current system characterized by short-time scale eddy activity and large-amplitude meanders (Qiu and Chen 2005; Kelly et al. 2010). At the same time, the KE has a key role in determining the substantial decadal variability of the Pacific climate through its prominent quasi-decadal SSH fluctuations (Pierce et al. 2001; Kwon and Deser 2007; Kwon et al. 2010; Qiu et al. 2014).

Previous studies have focused on understanding low-frequency KE variability because the decadal KE modulations are linked to changes in important physical dynamics of the western boundary current (WBC) system (e.g., Qiu and Chen 2005, 2010; Taguchi et al. 2007, 2010; Qiu et al. 2014). In particular, Qiu et al. (2014) have demonstrated that the decadal transitions of KE variability described by SSH variations (i.e., area-averaged SSH anomalies over 31°–36°N, 140°–165°E) can effectively explain the decadal changes in the latitudinal position of the oceanic jet, the length of eastward transport, and the strength of the southern recirculation gyre over the WBC system. While sea surface temperature (SST) is mainly modulated by sea surface heat fluxes, rapidly dissipating on seasonal time scales (Qiu and Kelly 1993; Kelly and Qiu 1995; Deser et al. 2003), the SSH, which is more related to ocean circulations and oceanic heat content, tends to have a longer memory of climate time scales (Sutton and Mathieu 2002; Kelly et al. 2010; Na et al. 2018). Because the KE SSH variability is one of the most dominant modes of large-scale variability in the North Pacific region and contributes a substantial fraction of the Pacific decadal variance (Schneider and Cornuelle 2005;

Denotes content that is immediately available upon publication as open access.

Supplemental information related to this paper is available at the Journals Online website: https://doi.org/10.1175/JCLI-D-21-0471.s1.

Corresponding author: Youngji Joh, youngji.joh@princeton.edu

DOI: 10.1175/JCLI-D-21-0471.1

Qiu et al. 2007; Kwon and Deser 2007; Anderson 2019), the degree of realism in the decadal KE state in global coupled climate models is crucial for understanding and projecting long-term changes in midlatitude air–sea coupled systems.

The ability of climate models to reproduce KE decadal variability may arise from the robust physical mechanisms driving and maintaining the low-frequency component, currently well established as an air–sea coupled system. The processes that affect the decadal KE system encompass regional ocean–atmosphere interactions, including oceanic advection (Qiu and Kelly 1993; Qiu 2000; Kelly and Dong 2004), local atmospheric forcing with related surface heat fluxes (Nakamura et al. 1997; Frankignoul and Kestenare 2002; Park et al. 2005; Linkin and Nigam 2008), and reemergence mechanism (Alexander and Deser 1995). In addition, remote atmospheric forcing over the central midlatitude North Pacific is especially known for modulating the KE dynamics on a longer time scale (Frankignoul et al. 1997; Miller et al. 1998; Deser et al. 1999; Seager et al. 2001; Schneider et al. 2002; Qiu 2003; Taguchi et al. 2007; Sasaki et al. 2013).

The remote wind stress curl anomalies ($\nabla \times \boldsymbol{\tau}$) have long been described as the evident forcing of KE decadal variability, where the KE is modulated by wind-driven, large-scale oceanic Rossby waves that convey the SSH anomalies from the central North Pacific to the WBC system. Observational and statistical analyses and numerical simulations have shown that westward-propagating baroclinic Rossby waves are associated with the natural variability of the North Pacific atmosphere (e.g., Latif and Barnett 1994 1996; Deser et al. 1999; Schneider and Miller 2001; Qiu et al. 2007; Taguchi et al. 2007 2010; Kwon et al. 2010; Sasaki et al. 2013). Specifically, changes in the intensity and location of North Pacific atmospheric wind forcing [i.e., the Aleutian low or North Pacific Oscillation (NPO)] are primarily responsible for the midlatitude anomalous SSH movement through Ekman transport divergence and convergence (Latif and Barnett 1994; Alexander and Scott 2008; Ceballos et al. 2009). The tropical atmospheric influences, however, cannot be excluded because the El Niño–Southern Oscillation (ENSO) teleconnections significantly alter the surface winds and fluxes of heat and momentum, which in turn impact SST, mixed layer, and oceanic currents of the North Pacific Ocean (Trenberth et al. 1998; Alexander et al. 2002; Liu and Alexander 2007). Although the question of how much the KE decadal variance is explained by separate tropical and extratropical forcing remains unclear, the robust finding that the midlatitude wind forcing drives decadal changes in the KE 2–3 years in advance certainly suggests the possibility of skillful KE forecasts.

Compared to existing forecasts for the other major climate modes (e.g., ENSO, Pacific decadal oscillation, Atlantic meridional overturning circulation, etc.), which have been extensively investigated and validated using fully coupled numerical simulations, the KE forecast skill has been mostly confined to a linear baroclinic Rossby wave model or Hovmöller diagrams of the zonal band of KE SSH anomalies (31°–36°N) (e.g., Qiu 2003; Qiu et al. 2007, 2014). While these empirical analyses have provided a dynamic framework to explore the KE prediction, they are limited by their inability to resolve related variables in their analyses (i.e., covarying atmospheric/oceanic variability in all dimensions), restricting in-depth investigation of the KE dynamics in the context of large-scale North Pacific variability.

Previous studies have explicitly and implicitly demonstrated the potential necessity of skillful KE forecasts in capturing the integrated dynamics of the entire regional WBC system and its impact (Zhou et al. 2015; Piazza et al. 2016; Ma et al. 2015, 2017; Morioka et al. 2019; Joh and Di Lorenzo 2019; Siqueira et al. 2021). For an examination of impacts and mechanisms of the KE system, several studies have suggested that a high-resolution ocean model ensemble approach (i.e., eddy-resolving, 0.1°, or eddy-permitting, 0.25°) is essential for building accurate detection and prediction of the turbulent eddy activity and related atmospheric/oceanic feedback (Piazza et al. 2016; Zhou et al. 2015; Ma et al. 2017; Siqueira et al. 2021). On the other hand, for KE prediction, the successful decadal KE forecasts using linear Rossby wave models imply that midlatitude large-scale SSH changes are largely governed by linear baroclinic vorticity dynamics and effectively account for the temporal evolution of the low-frequency KE variability (Qiu 2002; Taguchi et al. 2007; Qiu et al. 2014; Nonaka et al. 2016). Midlatitude atmospheric forcing excites basin-scale oceanic Rossby waves, enabling skillful predictions of large-scale SSH variability with even a relatively coarse horizontal model grid. In relation to a constraint of limited computational resources, examining how the different approaches or configurations of the coupled climate system (e.g., data assimilations and ocean model resolutions) reproduce and predict the KE dynamics could provide essential information for diagnostic discussion on the Pacific WBC system. If simple configurations confirm skillful KE predictions, these would facilitate efficient monitoring of the KE system and, more importantly, make it possible to investigate coherent large-scale atmospheric and oceanic circulations that were previously absent in statistical-dynamical models.

This paper investigates the representation and prediction skill of KE variability on a decadal and seasonal time scale using a new coupled prediction system named SPEAR (Seamless System for Prediction and Earth System Research) at the Geophysical Fluid Dynamics Laboratory (GFDL). Decadal and seasonal reanalysis systems with different approaches and corresponding retrospective forecasts are described in section 2. In section 3, we present the spatiotemporal representation of the KE and discuss the different approaches of data assimilations in reproducing the low-frequency component of the KE. We then evaluate the prediction skill of decadal KE fluctuations using SPEAR prediction systems, showing that both decadal and seasonal forecast systems exhibit significant long-lead predictability of KE SSH fluctuations in agreement with the observation satellite. At the end of section 3, we elucidate the mechanism of KE predictability in connection with the coupled air–sea processes of the North Pacific Ocean and suggest that a strong seasonality of midlatitude wind forcing plays an important role in maintaining the long-term ocean memory, leading to skillful long-lead KE forecasts (~1 yr for seasonal and ~5 yr

TABLE 1. Summary of reanalysis products designed for SPEAR forecasts. Both systems use the SPEAR_LO model [100-km atmosphere and 1° ocean resolution; more details in Delworth et al. (2020)]. [JRA = Japanese Reanalysis (Kobayashi et al. 2015); ERSSTv5 = NOAA Extended Reconstructed Sea Surface Temperature version 5 (Huang et al. 2017); OISSTv2 = Optimum Interpolation Sea Surface Temperature version 2 (Reynolds et al. 2002); EAKF = ensemble adjustment Kalman filter (Zhang et al. 2007). All models use the SPEAR coupled simulations with CMIP6 historical (1851–2014) and future projected radiative forcing SSP5-8.5 (2015–2100; Delworth et al. 2020).]

GFDL SPEAR reanalysis systems	RS-ATMSST	ODA
1958–2020	1990–2019	
Atmospheric initialization	Restoring air temperatures and winds to JRA reanalysis	No atmospheric restoring in long run with subsurface ocean assimilation
Ocean initialization	Restoring SST to ERSSTv5 no subsurface assimilation	Surface and subsurface assimilations (EAKF) Daily OISSTv2, Argo, XBT and tropical moorings
Ensemble members	30	30
Reference	Yang et al. (2021)	Lu et al. (2020)

for decadal prediction). The related potential applications to regional impact over the Pacific region are discussed in section 4.

2. Model, datasets, and methods

a. SPEAR model

SPEAR, a new seasonal-to-decadal modeling and prediction system developed by the GFDL, consists of the AM4-LM4 atmosphere/land model (Zhao et al. 2018a,b), MOM6 (https://github.com/NOAA-GFDL/MOM6) ocean model (Adcroft et al. 2019), and SIS2 sea ice code (https://github.com/NOAA-GFDL/SIS2) with the ability to run large ensemble simulations. The SPEAR model shares many components of the recently developed GFDL CM4 and offers different options for atmospheric horizontal resolutions ranging from 1° to 0.25°, depending on the interests of research and prediction. Here we use a low-resolution configuration (SPEAR_LO; 1° atmosphere and land) to produce large ensembles and data assimilation due to efficient computational speed. We also utilize a medium-resolution model (SPEAR_MED; 0.5°) that is designed to resolve weather extremes or short-time climate variability (e.g., hurricanes, thunderstorms, extratropical storms, and snowpack). The ocean model resolution is approximately 1° (with tropical refinement) in all configurations. The details of the configurations and physical parameterizations of the SPEAR can be found in Delworth et al. (2020).

b. Reanalysis systems designed for decadal and seasonal forecasts

Two coupled reanalysis products are developed for initializing SPEAR forecasts. Both reanalysis systems are provided by combining the time-varying coupled states with observational data assimilation. In the first coupled reanalysis system (RS-ATMSST in Table 1), atmospheric winds and temperature are restored toward 6-hourly Japanese 55-Year Reanalysis (JRA-55; Kobayashi et al. 2015), and SST is restored toward the time-varying observations from NOAA Extended Reconstructed Sea Surface Temperature version 5 (ERSSTv5) (Huang et al. 2017). By restoring time-dependent atmospheric observations and SST, the model ocean surface experiences a similar sequence of air–sea heat and momentum fluxes as the real ocean. As a result, the model ocean may respond dynamically in a way similar to the observed ocean, even without direct subsurface ocean data assimilation (Yang et al. 2021).

The second coupled reanalysis system (ODA in Table 1) solely uses ocean data assimilation without atmospheric observations. The assimilated ocean observations include daily NOAA Optimum Interpolation Sea Surface Temperature version 2 (OISSTv2) (Reynolds et al. 2007), Argo temperature and salinity data (Argo 2019), daily Global Tropical Moored Buoy Array temperature (https://www.pmel.noaa.gov/gtmba/), and XBT (expendable bathythermograph) data from the Global Temperature and Salinity Profile Programme (GTSPP) (Sun et al. 2010). While the ocean component is constrained by these above observations and the sea ice component indirectly communicates with the assimilated SST, the atmosphere and land components freely evolve given the ocean and sea ice boundary conditions. More descriptions about ODA are documented in Lu et al. (2020) (referred to as SPEAR Ocean Data Assimilation system, SPEAR_ODA).

The different reanalysis systems described above share the same radiative and aerosol forcing. Before 2014, observed estimates of changes in greenhouse gases, natural and anthropogenic aerosols, solar irradiance, and land-use changes are used to force the model. From 2015 onward, radiative forcing changes from the Shared Socioeconomic Pathway 5–8.5 (SSP5–8.5) are applied to the model. See Delworth et al. (2020) for further details on the radiative forcing. Both initializations are conducted as an extensive ensemble set of 30 members. RS-ATMSST and ODA are run for the period 1958–2020 and 1990–2019, respectively.

c. Retrospective forecasts

SPEAR forecasts for the decadal and seasonal prediction of KE SSH are evaluated at different lead times (DRF and SRF in Table 2). The decadal reforecast system (DRF) is initialized from RS-ATMSST, where time-varying atmospheric components and SST are restored to observations as initial conditions, but no subsurface ocean data assimilation is

TABLE 2. Description of the SPEAR coupled forecast system for the decadal and seasonal predictions. All models use the SPEAR coupled simulations with CMIP6 historical (1851–2014) and future projected radiative forcing SSP5-8.5 (2015–2100) (Delworth et al. 2020).

GFDL SPEAR prediction system	Decadal retrospective forecast (DRF)	Seasonal retrospective forecast (SRF)
Model	SPEAR_LO (Delworth et al. 2020)	SPEAR_MED (Delworth et al. 2020)
Atmosphere resolution	100 km	50 km
Ocean resolution	1° (1/3° in the tropics)	1° (1/3° in the tropics)
Initialization month	1 January	First of each month
Forecast length	10 years	1 year
Time period considered	1961–2021	1992–2021
Atmos., land, and sea ice initial condition	From RS-ATMSST	From SPEAR_MED_nudged (Lu et al. 2020)[a]
Ocean initial condition		From ODA
Ensemble member	20	15
Reference	Yang et al. (2021)	Lu et al. (2020)

[a] Restoring temp, wind, and humidity to NOAA/NCEP CFSR (Saha et al. 2010) and restoring SST to OISSTv2.

utilized. Each DRF member is initialized on 1 January every year from 1961 to the present (i.e., 2021) and integrated for 10 years (120 months). A set of reforecasts with 20-member ensembles is conducted. Significant forecast skill of DRF in the prediction of North Atlantic subpolar gyre SST, the multidecadal SST trend, and Sahel precipitation can be found in Yang et al. (2021).

For the seasonal reforecast system (SRF), while the ocean initial conditions are from ODA, the atmosphere, land, and sea ice initial conditions are from a separate ensemble of runs, SPEAR_MED_nudged in Lu et al. (2020). In the SPEAR_MED_nudged experiment, the air temperatures, winds, and humidity are restored to the 6-hourly data from the Climate Forecast System Reanalysis (CFSR; Saha et al. 2010) and SST restored to the daily observations from Optimum Interpolation Sea Surface Temperature (OISST; Reynolds et al. 2007). The details of the SPEAR_MED_nudged run can be found in Lu et al. (2020). SRF is initialized on the first of each month from 1992 to the present (i.e., 2021 January), and each forecast is integrated for 1 year (12 months) with 15 ensemble members.

d. Observational datasets

Sea surface height initializations and retrospective forecasts are validated against monthly averages of 0.25° global SSH datasets of SSALTO/DUACS altimetric mean dynamic topography distributed by the Copernicus Marine and Environment Monitoring Service (CMEMS). To examine the KE-related atmospheric variability, we use monthly sea level pressure from the National Centers for Environmental Prediction–National Center for Atmospheric Research (NCEP–NCAR) reanalysis (Kalnay et al. 1996).

e. Predictability and prediction skill

In this study, predictability indicates the potential ability to predict, when given a perfect physical model and accurate initial conditions. Predictability assesses whether a certain phenomenon can be theoretically predicted or not. In contrast, prediction skill assesses the actual accuracy of real-world predictions, given an imperfect model, limited observations, and imperfect initialization methods.

f. Prediction skill evaluation

Before evaluating the KE prediction skill from the reforecast systems, we compute forecast anomalies by removing the lead-time-dependent forecast climatology (i.e., different base periods for different forecast systems), where the climatological averages are obtained as monthly means of each lead time and grid point from the raw forecast. This process eliminates the related forecast bias such as climate drift that may derive from a systematic model error, where the climatology of the model is different from the observed climatology (i.e., Yang et al. 2013; Meehl et al. 2014; Yang et al. 2018; Jacox et al. 2019). Also, to optimize the predictive skill, we apply the trend correction that adjusts a time-dependent trend by fitting linear trend coefficients for each forecast lead time (Kharin et al. 2012). Specifically, to correct a difference between the observed and modeled long-term trends, the modeled long-term trend is replaced with the observed one. To compute the linear trend corrections, we use the standard least squares method depending on both lead time and the initial year. We measure the forecast skill with the anomaly correlation coefficients (ACC) between forecasted and observed fields, as is widely used in previous studies (i.e., Stock et al. 2015; Jacox et al. 2019; Yang et al. 2021). We develop a damped persistence model, known as the CLIPER (climatology and persistence) forecast (Knaff and Landsea 1997). In this study, we define "significant skill" as the forecast skill above persistence (e.g., when the ACC are higher than CLIPER forecast) and also when it is statistically significant (10% level) based on the Monte Carlo approach. In the Monte Carlo method, we generate large sample sets realizations (e.g., 6000) of an ensemble with 30 random pairs of time series that contain the same characteristics of the observed KE index [e.g., the same time steps (N), mean, standard deviation, and autocorrelation] using the first-order autoregressive model. For the statistical significance calculations, the degrees of freedom are adjusted following Panofsky and Brier (1958) due to the red noise component of the KE index. The effective degrees of freedom are determined as

$$N_{\text{effective}} = N(1 - \alpha)/(1 + \alpha),$$

where N is the length of the time steps and α is the lag-1 autocorrelation.

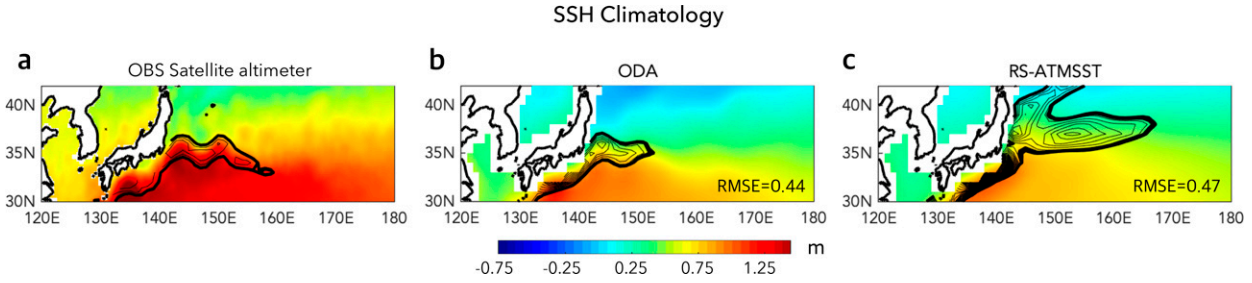

FIG. 1. Annual mean SSH climatology for the period of 1993–2019 from (a) the observation satellite, (b) ODA, and (c) RS-ATMSST. The 30-member ensemble means from the reanalysis system are shown. The KE oceanic jet measured by strong meridional SSH gradient (above two standard deviations of global $\partial SSH/\partial y$) is denoted as a solid black contour [1 m for (a); 0.5 m for (b) and (c)] with an interval of 0.1 m. Area-averaged RMSE (root-mean-square error) of reanalyses are shown at the bottom right in (b) and (c).

3. Results

a. *KE representation in SPEAR coupled reanalysis systems*

We examine the representation of spatial characteristics of the KE system, including the mean state and variability of the KE SSH using the observation satellite altimeter and SPEAR reanalysis large ensemble (i.e., 30 members of RS-ATMSST and ODA) (Figs. 1 and 2). Figure 1 shows a comparison of the horizontal climatological SSH gradient between the observed and simulated patterns. The observation (Fig. 1a) and ODA (Fig. 1b) show similar latitudinal positions of the KE jet and its meanders, whereas RS-ATMSST (Fig. 1c) exhibits a less meandering jet with a northward displaced position with respect to observation and ODA of ~2°. A difference in the position and structure of the oceanic jet simulated by the two systems suggests that the subsurface ocean data assimilation (i.e., subsurface observations) is essential to detect the accurate KE axis via the observational temperature and salinity that constrain ocean circulation through thermal wind relationship, especially for the ocean component model with 1° horizontal resolution. Partially, the resolution of the SST observations used in the data assimilation may also affect the simulation of the KE jet because ODA uses much higher resolution observed SST constraints than RS-ATMSST (i.e., 0.25° OISSTv2 for ODA vs 2° ERSSTv5 for RS-ATMSST; Table 1), in that the restored or assimilated SST observation with high-resolution can contain the impact of intrinsic oceanic mechanisms on the KE, such as mesoscale eddy activity. As for the common model bias detected in the two different simulations, both simulated annual mean SSH patterns show a weaker SSH gradient across the western North Pacific than in the satellite altimeter observations, which might be associated with insufficient mesoscale eddy activity to the relatively coarse horizontal resolution of the current ocean model. SSH

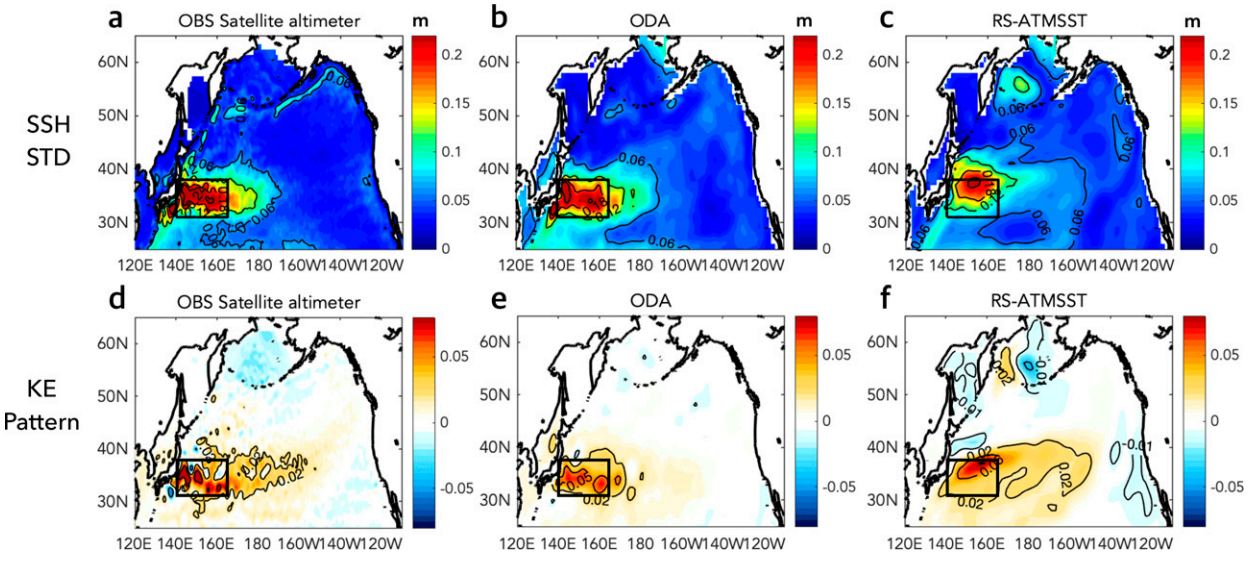

FIG. 2. North Pacific SSH variability and KE pattern for the period of 1993–2019. Standard deviation of SSH anomalies from (a) the observation satellite, (b) ODA, and (c) RS-ATMSST. (d)–(f) As in (a)–(c), but for the KE pattern (m) as the regression coefficient between the SSH anomaly field with the normalized KE index (area-averaged SSH anomalies over 140°–165°E and 31°–38°N, denoted as a black box).

biases can also stem from zonal wind stress biases (i.e., Lee et al. 2013; Landerer et al. 2014). The relatively coarse horizontal resolution of the atmosphere models may result in insufficient wind forcing spatial peaks that affect the SSH gradient.

In Fig. 2, SSH standard deviations show the exceptionally strong SSH variance over the KE region in both observation and models. Compared to observation, climate models underestimate the KE SSH interannual fluctuations. ODA exhibits a very similar SSH standard deviation pattern as observed regarding the spatial structure and location of the maximum SSH (cf. Figs. 2a,b). On the other hand, RS-ATMSST shows the intensification of KE jet overshoot that takes a northward displaced position compared to the observed (cf. Figs. 2a,c). We next present regression maps (Figs. 2d–f) computed by SSH anomalies with the KE index [area-averaged SSH anomalies over the KE region (140°–165°E and 31°–38°N)]. In this study, the definition of the KE region is slightly different from Qiu et al. (2014) to cover the region showing the strong SSH variability (Fig. S1 in the online supplemental material) and the region of KE jet overshoot in RS-ATMSST. A comparison of the KE pattern between the observation and models reveals (Figs. 2d–f) that the relatively coarse horizontal resolution of the current ocean model may not accurately represent the narrow frontal variability of the KE jet, especially when the simulated oceanic fields are not constrained with subsurface observations (cf. Figs. 2d,f). In contrast, compared to ODA, RS-ATMSST appears to more reasonably capture the observed basin-scale signatures of the KE variability, such as the strong eastward KE path (cf. 0.02 contour lines of Figs. 2d,f) and the local negative anomalies over the northern and eastern part of the North Pacific Ocean (Figs. 2d,f). This dissimilarity of the reproducibility between ODA and RS-ATMSST may arise from insufficient observational constraints in the ODA (e.g., sparse Argo availability or/and no atmospheric data assimilation). A recent study (Fedele et al. 2021) points out that while the upstream KE region (~140°–153°E) is associated with eddy–mean flow interactions as an oceanic front of the WBC (i.e., highest eddy kinetic energy; Fig. 2a in Fedele et al. 2021), the downstream KE (~153°–165°E) is more influenced by the basin-scale air–sea coupling linked to the extratropical North Pacific variability (e.g., Pacific decadal oscillation). Consistent with this, our findings suggest that the ocean assimilation and restoring atmospheric components each may contribute to improving the SSH representations of the upstream and downstream region, respectively.

We next illustrate in Fig. 3 the evaluation of the temporal evolutions of the KE low-frequency component. We first compute ACC between observed and simulated SSH evolutions in Figs. 3a and 3b. For computing ACC, both models and observation are regridded to $1° \times 1°$. Correlations that are not statistically significant at the 10% level are not colored (denoted as white). In general, the SSH variability estimated from ODA and RS-ATMSST agrees well with the variability observed by satellite altimeter over the majority of the Pacific region with correlations above 0.75 (Figs. 3a,b). Overall, the correlation coefficients range mostly from 0.75 to 0.95 except for the western North Pacific, where mesoscale eddy activity is highly important. The WBC region exhibits little agreement between the models and observation at many grid points, showing statistically insignificant correlations. We note however that in both ODA and RS-ATMSST the KE region shows relatively higher agreement with the observation than the rest of the other WBC regions ($R > 0.55$; zoomed-in box in Figs. 3a,b). Consistent with this, we find that the estimated SSH-based KE indices from both reanalyses strongly overlap with the observed one, showing a high correlation ($R = 0.90$, $p < 0.01$) with the observation since 1993 (Fig. 3c). However, the detection of the temporal evolution of KE SSH on both interannual and decadal time scales in RS-ATMSST cannot indicate the existence of adequate ocean dynamic properties of the KE system (e.g., KE position and recirculation gyre strength) because the KE SSH evolution of RS-ATMSST is mostly contributed by the encompassed observed KE SSH through restoring SST and atmospheric anomalies, not induced by the actual KE jet variability including the impact of ocean circulation or transport. Nevertheless, the strong agreement in the KE fluctuations between the models and the satellite altimeter suggests that these reanalysis systems can be used as an important tool for long-term KE examination beyond the satellite era (the period before 1992) as an extended observation. In addition, as confirmed in previous studies, both the observed and simulated KE indices show the prominent quasi-decadal preferred time scale (~10 yr) for the recent decades in their power spectra (Fig. 3d) (Qiu et al. 2007; Joh and Di Lorenzo 2019; Anderson 2019; Siqueira et al. 2021). We especially note that the ODA coupled run without atmospheric assimilation shows an appreciable ability to represent the observed KE time scales (black line in Fig. 3d). This suggests that the contribution of wind anomalies (e.g., midlatitude wind forcing of oceanic Rossby waves) or changes in pycnocline and corresponding low-frequency SSH variability are adequately constrained by the assimilation of subsurface observations, which enables ODA to detect the atmospherically forced decadal variability of the KE. The representation of the KE pattern in ODA appears to be improved, especially over the central North Pacific region, for the recent period (e.g., after the mid-2000s) due to the full development of subsurface observations such as Argo (not shown). Collectively, we confirm that both reanalysis products with different initialization approaches (atmospheric/SST restoring vs ocean data assimilation) have the capability to reproduce the accurate temporal evolution of KE SSH fluctuations, which are comparable to the observation satellite. These reanalyses are used to generate initial conditions for SPEAR prediction systems. We next examine the prediction skill of the KE variability using decadal and seasonal retrospective forecasts.

b. SPEAR forecast systems for KE prediction

1) DECADAL FORECAST

In this section, we explore KE prediction skills through decadal (DRF) and seasonal (SRF) prediction systems

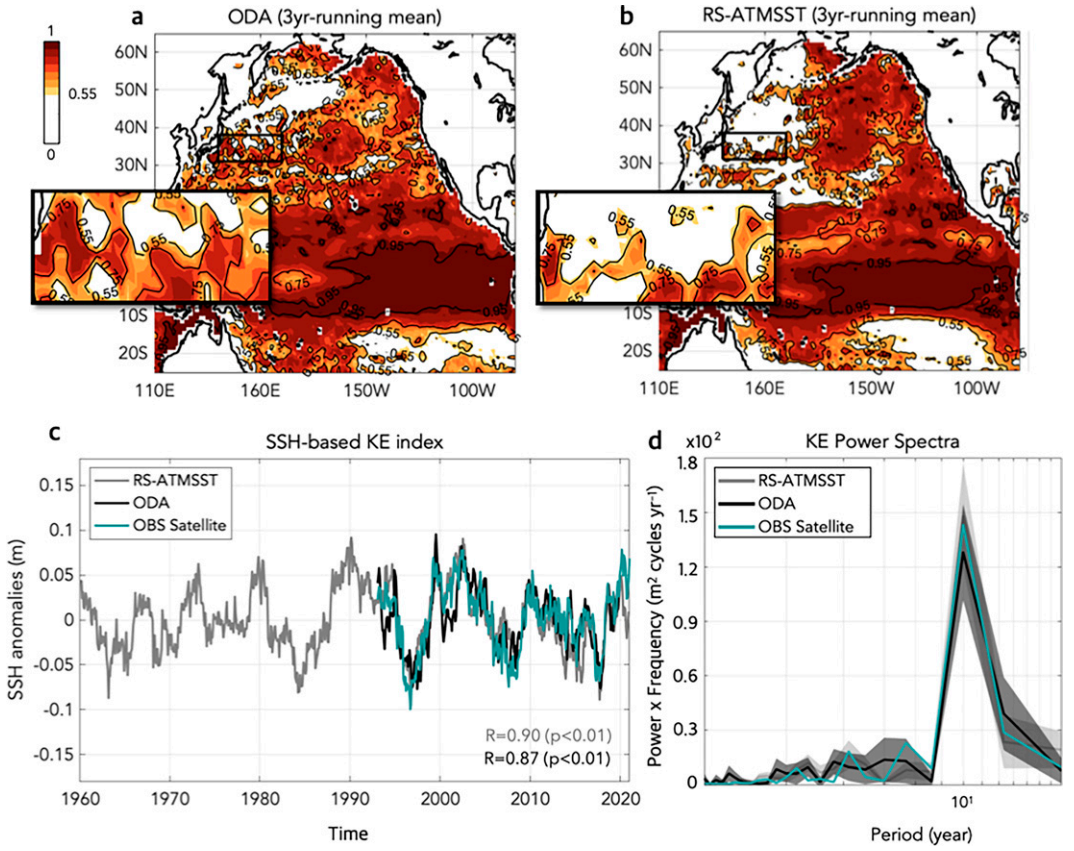

FIG. 3. North Pacific SSH evolution and temporal characteristics of the KE SSH. (a),(b) ACC of SSH time series (the 3-yr running mean) at each grid point between the observation satellite with (a) ODA and (b) RS-ATMSST for the period of 1993–2019. Models and observations are regridded to 1° × 1°. Correlations below 90% level are denoted as white based on Student's *t* test. The KE region is zoomed in on the extra black box next to the main panel. (c) Observed and simulated SSH fluctuations over the KE region, as measured by the KE index. The correlations between the observed and the simulated KE index are shown at the bottom right (R = 0.90 with RS-ATMSST; R = 0.87 with ODA). (d) Power spectra of KE index from observation and reanalyses for the period of 1993–2019. The shading denotes the 95% ensemble range.

initialized by the reanalysis system of RS-ATMSST or ODA (see details in Table 2). We first examine the significance of DRF KE forecasts by comparing performance with that of the KE persistence. In nature, due to the large thermal inertia of the ocean, the oceanic variables, especially SSH, evolve very slowly, having longer memory than the atmosphere. The SSH-based KE index thus also has a strong persistence (i.e., high autocorrelation) with little month-to-month change. The damped persistence is widely used in prediction research (Qiu et al. 2007, 2014; Jacox et al. 2019). The significant correlations of the dynamical climate forecast above persistence can provide information regarding the underlying mechanism and the related predictability.

The KE persistence forecasts and evaluations of decadal KE prediction skills are summarized in Fig. 4a. Autocorrelations of the KE index show that the memory of KE appears to come mostly from the phase transition of its decadal time scale oscillation (~10 yr; bars in Fig. 4a). The CLIPER forecasts skill reveals that the persistence skill is not statistically significant after lead year 2, showing that the forecast drops below 0.5 after 2 years and becomes statistically nonsignificant. The correlations between the predicted and observed KE indices are shown as a function of lead time (in years). We use both reanalysis (RS-ATMSST, a black line) and the satellite altimeter (OBS, a green line) as the references to compare with forecasts. The dynamical forecast shows significant correlations above both the CLIPER forecast and the Rossby wave adjustment KE prediction skill [green dashed line, adopted from Qiu et al. (2014)] up to lead time 5 years in both cases (bold lines in Fig. 4a). Particularly, for the lead times of 1–3 years, the KE forecasts exhibit a relatively small ensemblespread (i.e., less uncertainty), showing significant correlations in all the individual members at the 5% level compared with reanalysis (black dashed lines in Fig. 4a). After lead times of 4 years, the ensemble spread dramatically increases with a minimum correlation of ~0.2, indicating that the prediction skill largely varies between individual ensemble

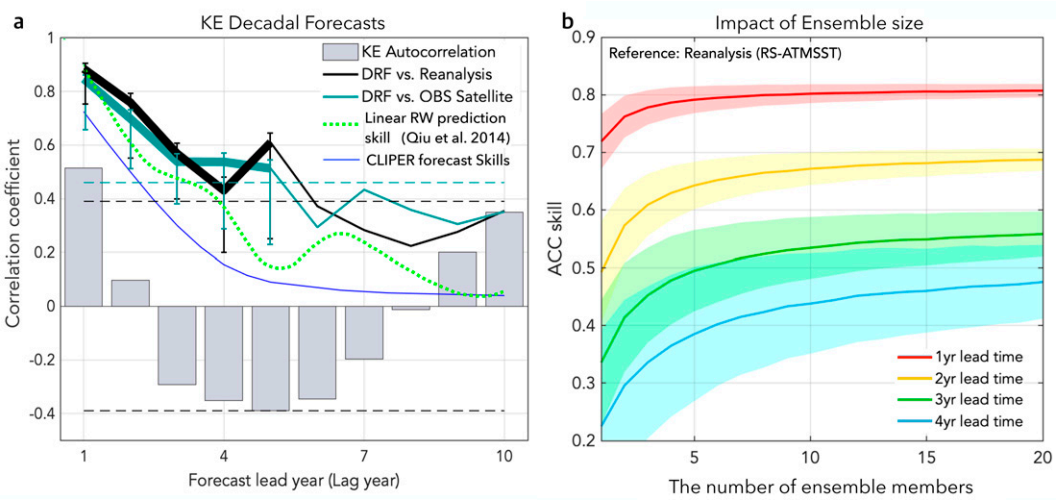

FIG. 4. Measures of decadal forecasts of KE SSH from SPEAR decadal prediction system (DRF). (a) ACC are compared to the persistence forecast (autocorrelation; bars). The black line indicates the ensemble mean correlations between the forecast and the reanalysis (RS-ATMSST) for the period of 1961–2020. The green line indicates the ensemble mean correlations between the forecast and satellite altimeter for the period of 1993–2020. Significant correlations above the 5% level (dashed lines) based on a Monte Carlo approach are denoted as bold lines. The blue line represents CLIPER forecasts skill on damped persistence predictions. Prediction skill based on the linear Rossby waves model is denoted as a dashed light green line, adopted from Fig. 9 in Qiu et al. (2014), where the KE index is predicted based on Rossby wave adjustment and KE wind feedback (two-way scenario). In every forecast lead year, the full ensemble spread is denoted as a vertical bar. (b) Bootstrap test of ensemble size impact on ACC based on 5000 bootstrapped sets of ensembles. The line is ensemble mean ACC as a function of the number of ensemble members used in forecasts. The shaded area indicates the 90% ensemble range from the bootstrap distribution.

members. This result suggests that long-term KE prediction of more than 4 years has more uncertainty in forecasts, and a different selection of subsets of ensemble members or ensemble size may affect KE prediction skill.

To show the impact of ensemble size on ACC, we conduct the bootstrap test in Fig. 4b. A bootstrapping method is conducted by selecting a random subset of n forecast ensemble members and repeating 5000 times to produce a bootstrap distribution of the mean and range of forecast models for ensemble size from $n = 1$ to $n = 20$. In the bootstrapped set, the sampling is with replacement so that a given forecast ensemble member can be selected more than once. The average correlations between reanalysis (RS-ATMSST) and decadal forecast (DRF) are shown as a function of ensemble size. The mean of ACC from the bootstrapped forecasts indicates that the forecast skill increases rapidly for small ensemble sizes but quickly levels off for ensemble sizes exceeding 5–10 members, especially for the levels of skill shown for lead times of less than three years. Therefore, we find that an ensemble size of 20 is sufficient (nearly saturated) for nearly achieving maximum KE prediction skill for forecast lead times of 1–3 years. For the long-term KE forecasts with lead times of 4 years or more, however, it shows that ACC can improve by increasing ensemble size beyond 20. Taken together, using the SPEAR decadal prediction system, we confirm the potential of multiyear KE prediction with significant skill up to 5 years, especially highly reliable skill exceeding the range of the ensemble spread for up to 3 years.

In Fig. 5, we show reconstructed KE variability from DRF for the period of 1961–2020. From different forecast lead times ranging from 1 to 3 years, we compare the forecasted annual KE index, its power spectrum to RS-ATMSST, and the KE pattern. For 1–3-yr lead times, the reasonable prediction (R = 0.58–0.81) of annual KE variability is confirmed in the left column of Fig. 5. Also, the observed time scales of KE (~10 yr) are reasonably captured in the power spectra of KE forecasts, as shown in the middle column of Fig. 5. From the lead time of 2 years, the variance of KE appears to be slightly underestimated as shown in the power spectrum (Figs. 5e,h) and spatial pattern (Fig. 5f,i); however, we note that those spatiotemporal characteristics of KE forecasts show robust and consistent features across different forecast lead times, presenting the strong quasi-decadal oscillations (~10 yr) and apparent eastward KE jet signature.

2) SEASONAL FORECAST

We next examine KE prediction skills using the SPEAR seasonal forecast system (SRF). In Fig. 6, ACC are plotted as a function of forecast lead times and initialization seasons in comparison with two references: ODA reanalysis (top panels) and satellite altimeter dataset (bottom panels). The ACC with ODA (Fig. 6a) show significant forecast skill above persistence (i.e., CLIPER forecast) across all seasons up to 3-month lead times. On the other hand, the ACC with satellite data (Fig. 6c) exhibit no significant skill above persistence for a short-lead forecast. We attribute the statistically nonsignificant short-lead KE forecasts compared with

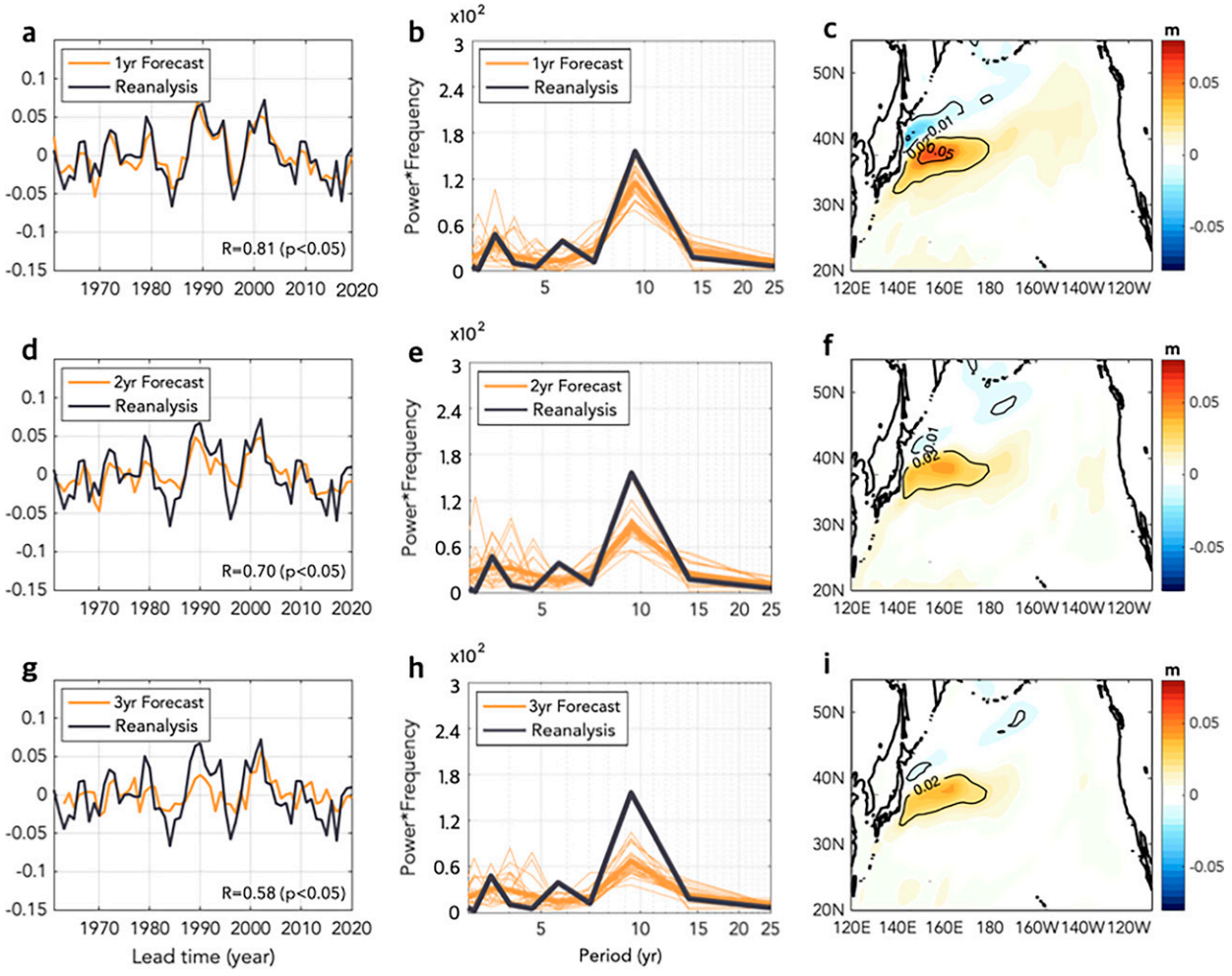

FIG. 5. Examination of KE spatiotemporal evolutions from DRF for the period of 1961–2020. (a) Time series and (b) power spectra of KE index from 1-yr lead time from DRF (a thick yellow line) and RS-ATMSST (a thick black line) are shown. For comparison with the observed power spectra (i.e., a single realization), the spectrum of each ensemble member is shown separately (thin yellow lines). (c) KE pattern (regression coefficient of SSH anomaly field with KE index) is reconstructed by DRF using 1-yr lead time. (d)–(f) As in (a)–(c), but for 2-yr forecast lead time. (g)–(i) As in (a)–(c), but for 3-yr forecast lead time. The 20-member ensemble means of DRF are shown in (a), (d), (g), (c), (f), and (i).

the observation satellite to the underestimated intrinsic ocean dynamics, which are generated by nonlinear oceanic mechanisms. As pointed out in previous literature (e.g., Fedele et al. 2021), relatively coarse-resolution ocean models would underestimate eddy kinetic energy near the ocean front and insufficiently capture the short-lived eddy activity or large-amplitude meanders compared to satellite altimeters. For the seasonal forecasts, thus which might suffer from the impact of this short time scale eddy activity, the short-lead KE prediction skills are found to be challenging in the current SPEAR model configuration (i.e., 50-km atmospheric and 1° ocean models). However, we note a consistent tendency across different reference data, where the lowest and highest long-lead KE prediction skill comes from forecasts initialized in the warm (May–October) and cold season (November–April), respectively (Figs. 6a,c). The skill for different initialization seasons is examined in Figs. 6b and 6d. We find that while the forecasts initialized in the warm season (April–September) exhibit less skillful long-lead prediction (red line in Fig. 6b) or lower ACC than the KE persistence (red line in Fig. 6d), the forecasts initialized in the cold season (November–March) generate the significant forecast skill above CLIPER forecasts, especially for long-lead forecasts (i.e., 4–11 months; blue lines in Figs. 6b,d). These findings suggest that KE seasonal forecast skill is both lead time- and initialization month-dependent, which will be explored further in section 3c.

A closer examination of seasonal KE forecast performance is shown in Fig. 7. We first find that short-lead KE forecast skills (red lines) are relatively constant across the different

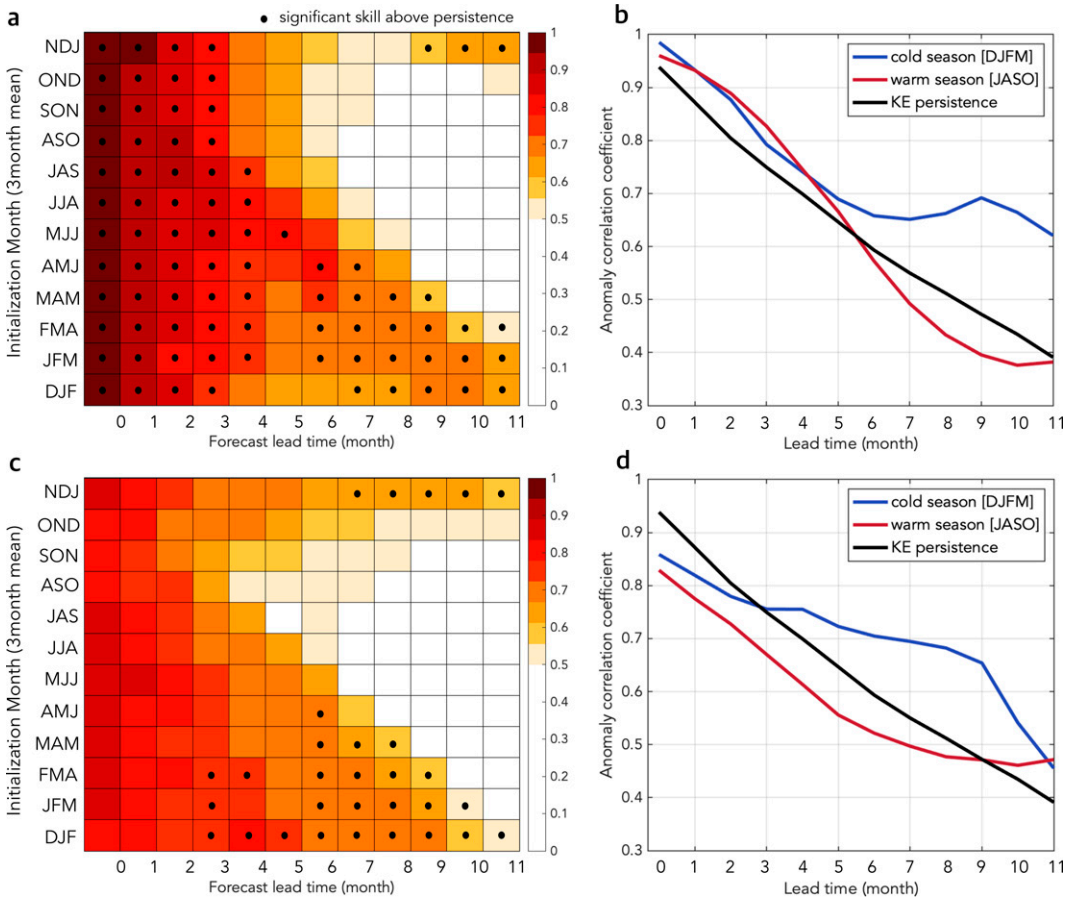

FIG. 6. Seasonal forecast skill of the KE SSH from SRF. ACC of the KE index with (a) ODA for the period of 1992–2019 and (c) the observation satellite for the period of 1993–2020 are shown. Forecast lead time is on the x axis, initialization season is on the y axis, and the ACC are in color. The forecast lead time of 0 is for the month of initialization. Dots indicate significant forecast skill above CLIPER forecasts. (b),(d) As in (a) and (c), but for ACC averaged by different season initialization. Skill is shown for CLIPER forecasts (black line) and KE forecasts from cold (December–March; blue) and warm (July–October; red) month initializations. The 15-member ensemble means from SRF are shown.

initialization months (Fig. 7a) and the forecast target month (Fig. 7b). However, we note that the long-lead forecast skills (blue lines) greatly vary with respect to month (blue lines in Figs. 7a,b). Specifically, the long-lead KE predictive skill is highest for winter initializations (December–February) and lowest for late spring to fall initializations (May–October; blue lines in Fig. 7a). The target month with maximum KE SSH forecast skill is September (Fig. 7b). This result is consistently confirmed in the different verification data (cf. dashed and solid lines in Figs. 7a,b). Simply put, by using prior January initializations, we can expect the best forecast skill for fall KE predictions.

As for the longer time-scale perspective, we find that the decadal fluctuations of KE variability are well predicted across all lead times (0–11 months), with statistically significant ACC above KE persistence ($R > 0.64$) (left column in Fig. 8). To investigate if the observed KE index can be regarded as any member of the forecast ensemble, we show a rank histogram (right column in Fig. 8). Rank histograms are used to evaluate ensemble forecasts by indicating the reliability of ensemble forecasts and diagnosing errors in their mean and spread (Hamill 2001). The rank histogram in Fig. 8 is generated by repeatedly counting the order of observation relative to the 15-member SRF ensemble as the distribution of frequency of the observation rank. Under the null hypothesis that the observations were produced by the same process as the model, the observations would appear with equal likelihood at any rank so that the rank histogram would tend toward uniformity (flatness) apart from fluctuations arising from the finite sample. The sample histogram can be tested for significant nonuniformity using a chi-square test. For lead times up to 3 months, the forecast ensemble indicates a U shape, which implies either biases or insufficient ensemble spread (i.e., underdispersion). The U-shaped rank histograms are often found in current forecasts due to an overconfident forecast ensemble, which implies that more than 30 ensemble members would be desirable for the short-term forecast

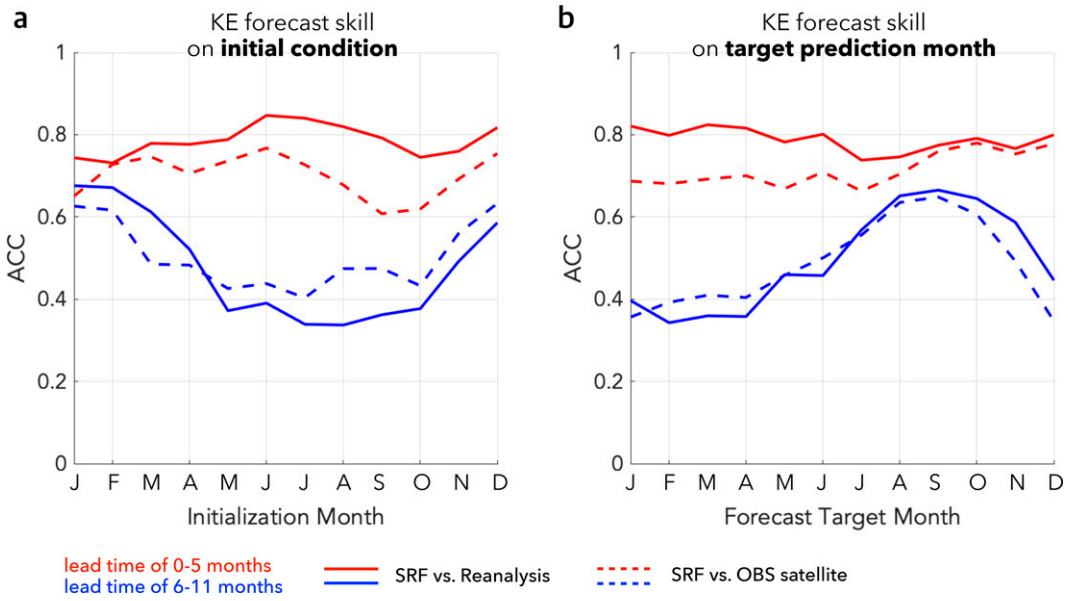

FIG. 7. ACC for forecasts of the KE index as a function of (a) initialization month and (b) forecast target month at short (0–5 months; red) and long (6–11 months; blue) lead forecast times. Verification data are ODA (solid) and the observation satellite (dashed). All panels are based on computations with the 15-member ensemble mean of SRF.

(~3 months). On the other hand, for lead times longer than 4 months, the rank histograms show a flat shape, which indicates the observation is statistically indistinguishable, where the observation can be considered as another ensemble member (i.e., reliable).

3) MECHANISMS OF KE PREDICTION SKILLS

Our findings shown in sections 3a and 3b highlight two key points: 1) significant KE (*based on the annual KE index*) forecast skill is found on time scales up to 5 years in the decadal prediction system (DRF) with January initializations. 2) Long-lead (4–11 months) skill (*based on the monthly KE index*) above persistence in the seasonal prediction system (SRF) is confined to winter initializations (December–February). To elucidate the mechanism behind KE forecast skill, we focus on the dominant mode of extratropical Pacific climate variability that strongly develops in boreal winter, which also has long been described as a crucial mechanism to modulate the decadal SSH variability over the WBC system (Frankignoul et al. 1997; Miller et al. 1998; Deser et al. 1999; Seager et al. 2001; Schneider et al. 2002; Qiu 2003; Qiu and Chen 2005; Taguchi et al. 2007; Ceballos et al. 2009; Sasaki et al. 2013). The first two dominant modes of North Pacific sea level pressure (SLP) variability and associated wind stress curl anomalies from RSATMSST reanalysis are shown in Fig. 9. The Aleutian low (AL; Trenberth and Hurrell 1994) and NPO (Walker and Bliss 1932; Rogers 1981; Linkin and Nigam 2008) are defined as the first (Fig. 9a) and second (Fig. 9b) leading empirical orthogonal functions (EOFs) of monthly SLP anomalies in the Pacific north of 20°N, respectively. As presented in Figs. 9a and 9b, when the phase of the dominant SLP modes has positive SLP anomalies over the midlatitude region, the intensified anticyclonic wind forcing results in an increase in positive SSH anomalies through the Ekman convergence over a large area of the western and central North Pacific, including the WBC system. This immediate oceanic response to wind forcing in the KE region can be detected in the cross-correlation function of the KE with PC1 (i.e., AL index, positive phase) and PC2 (i.e., NPO index, negative phase) at lag 0 (Figs. 9c,d). In Figs. 9c and 9d, the KE index and two PCs are computed as a 2-yr running mean. At a lag of 0 months, a statistically nonsignificant but positive correlation between the KE and PCs reveals that these basin-scale atmospheric forcings induce some fraction of the KE SSH variance with no lag time.

Meanwhile, we note that these midlatitude forcings significantly lead the KE by 20–30 months (Fig. 9d), consistent with previous findings that changes in intensity and location of the remote midlatitude wind forcing affect the WBC system via the baroclinic oceanic adjustment. A correlation map between the lagged meridionally averaged SSH anomalies and the two PCs, which is represented as the time–longitude section of 31°–38°N (KE band), exhibits similar signatures to large-scale oceanic Rossby waves. Consistent with Figs. 9c and 9d, a comparison of the two Hovmöller diagrams shown in Figs. 9e and 9f (AL vs NPO) reveals that the NPO-type variability is more significantly associated with the KE decadal SSH changes than AL, by generating more deterministic westward propagating Rossby wave signatures with larger SSH amplitude. The NPO-related negative anomalous wind stress curl over the central North Pacific (gray contours in Fig. 9b) is near the KE latitude band, and thus more effectively drives the wind-induced Rossby waves that propagate to the western

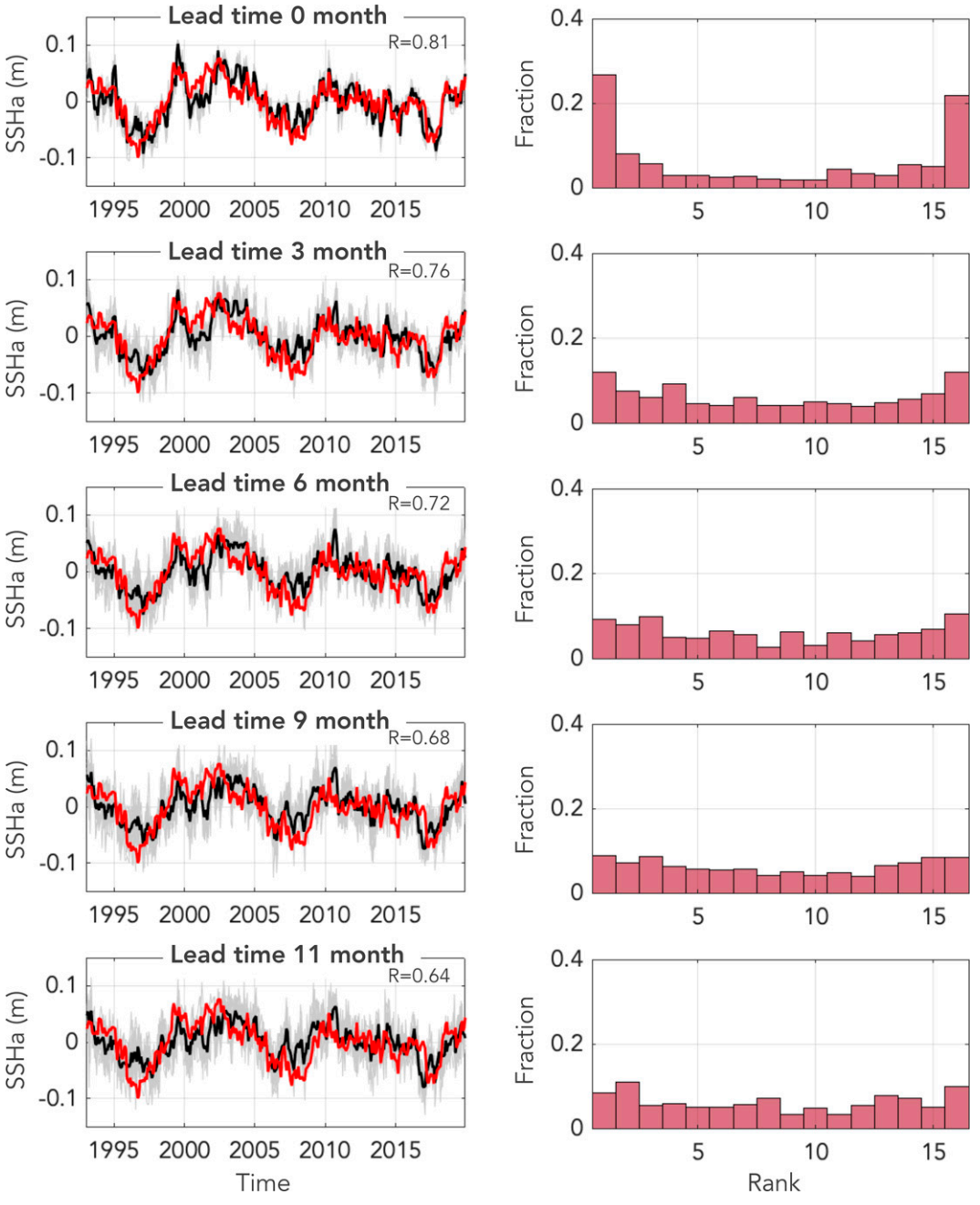

FIG. 8. Evaluations of SRF forecast skill KE SSH. (left) A comparison of the monthly KE variability between ODA and SRF. KE forecasts of ensemble mean (black) and individual member (gray) are compared with the observed KE index (red). ACCs between the observed and predicated KE index (ensemble mean) are shown at the top right in each panel. (right) Rank histograms of KE index forecasts as a distribution for the rank of observations relative to the 15-member SRF ensemble.

boundary and contribute to decadal KE SSH variability (black box) roughly 3 years later (arrows in Figs. 9e,f). However, we note that depending on the scale and location of the midlatitude wind forcing, the inertial memory of baroclinic Rossby waves could vary (Kwon and Deser 2007). In addition, when the Rossby waves are excited by strong, persistent wind forcing (up to 2–5 years; Fig. 11) over the midlatitude Pacific, the additional years of the predictable lead time of KE SSH variability could be provided, thereby allowing that the lead time of significant predictive skill (5 years in Fig. 4a) can be longer than the general time scales of the baroclinic Rossby waves (2–5 years) (e.g., Latif and Barnett 1994, 1996; Sasaki et al. 2013; Ceballos et al. 2009).

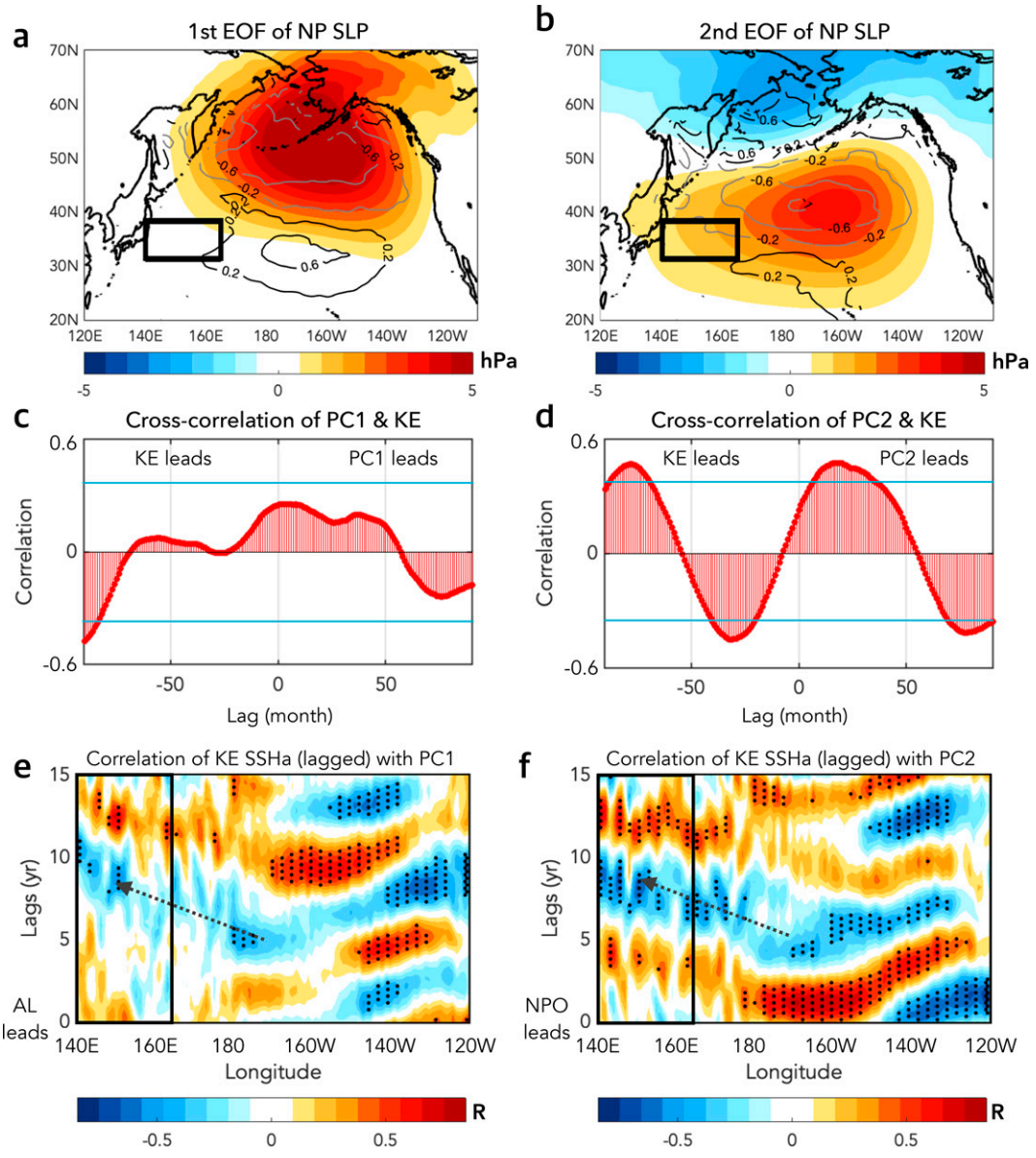

FIG. 9. Basin-scale North Pacific atmospheric forcing associated with the KE variability from RS-ATMSST for the period of 1958–2018. The first two dominant EOF patterns of North Pacific SLP (shading) are shown as (a) Aleutian low (AL; positive phase) and (b) North Pacific Oscillation (NPO; negative phase). Associated wind stress curl anomalies, which are regressed onto the AL and NPO time series (i.e., principal components) are denoted as contours (10^{-8} N m^{-3}), where the black and gray line each indicates the positive and negative anomalies. Cross-correlation function of KE index with the (c) first and (d) second principal component (i.e., PC1 and PC2), where all the indices are computed as a 2-yr running mean. Blue lines indicate the 5% level based on the Monte Carlo approach. Hovmöller diagrams of lag correlations between (e) PC1 and (f) PC2 and meridionally averaged SSH anomalies over the KE band (31°–38°N). All the indices are computed as a 2-yr running mean in the diagram. Stippling denotes grids where the correlation is significant at the 5% level based on Student's *t* test. The black box denotes the KE region defined in this study. Arrows indicate the direction of the westward propagations of oceanic Rossby waves.

East of 160°W, the SSH signals appear to propagate eastward at about 6 cm s^{-1}. The present study is concerned mainly with a communication between the WBCs system and the central Pacific, and we thus defer investigation of the causes of this east Pacific propagation to a future study. It is possible that this eastward propagation is associated with higher-mode baroclinic Rossby waves over the North Pacific (Taguchi and Schneider 2014; Nonaka and Xie 2000).

To examine the seasonal dependency of KE forecast skill, we investigate the seasonality of the NPO through the

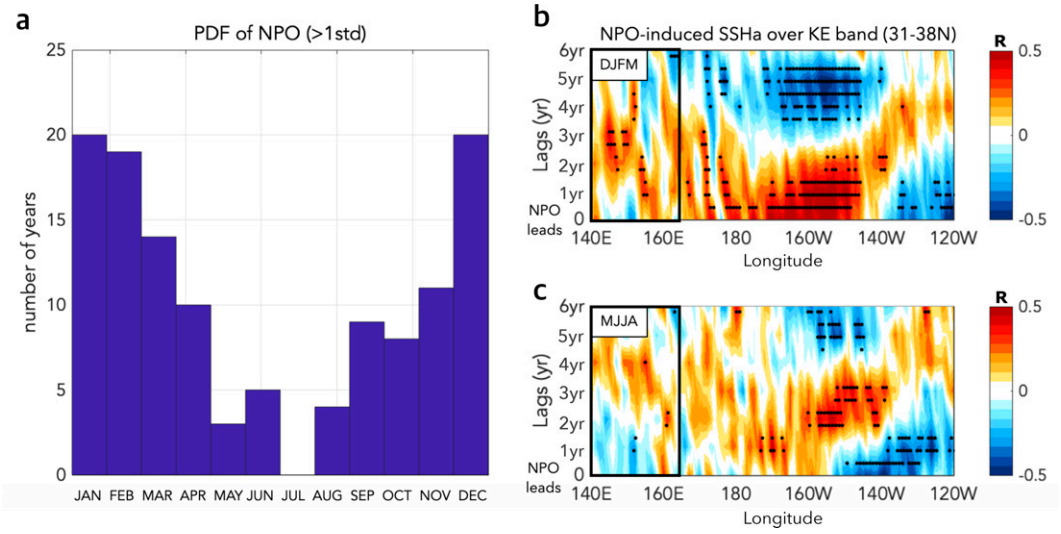

FIG. 10. Observed seasonality of NPO and the corresponding difference in SSH response over the KE band. (a) Distribution of the number of years when NPO amplitude is larger than one standard deviation, sorted by calendar month, for the period of 1948–2020. (b),(c) Hovmöller diagrams of lag correlations between the NPO index and meridionally averaged SSH anomalies over the KE band (31°–38°N) from 1993–2020. Annual SSH and NPO indices are used for the cold (December–March) and warm (May–August) seasons. The black box denotes the KE region. SLP and SSH anomalies are obtained from NCEP–NCAR reanalysis and the observation satellite (CMEMS), respectively. The dot denotes a grid where the correlation is significant at the 5% level based on the Student's *t* test.

distribution of NPO amplitude with respect to calendar months in Fig. 10a. We find that the NPO with larger variance (>1 standard deviation) is especially prominent during the winter seasons (December–February), where the stronger wind anomalies may play a more significant role in driving sea surface anomalies over the North Pacific. Supporting this, a comparison of Hovmöller diagrams between the cold and warm seasons reveals that the NPO forcing appears to impact the North Pacific Ocean more efficiently during the winter (cf. Figs. 10b,c). Compared to the warm seasons (May–August; Fig. 10c), the NPO during the cold seasons (December–March; Fig. 10b) drives the insignificant but stronger and wider direct SSH feedback over the KE region (at a lag of 0 years) and triggers larger-scale oceanic Rossby waves with stronger amplitude SSH anomalies (at lags of 0–3 years). We confirm that the SPEAR decadal prediction system resolves consistent SSH dynamics related to wind-induced remote forcing (Fig. 11), which implies that the decadal prediction skill may arise from the inertial memory of the upper ocean (i.e., large-scale oceanic Rossby waves). In Fig. 11, the transit time of the westward propagation from 180° to 140°E is about 2.5 years; thus, the phase speed of the anomalous SSH propagation is found to be approximately 4.6 cm s^{-1}, which is comparable to the observed phase speed of the first baroclinic mode Rossby wave in the North Pacific (Qiu 2003; Kwon and Deser 2007; Qiu et al. 2014). We suggest that winter initialization may contribute to the long-lead prediction skills through winter intensification of midlatitude atmospheric forcing as a crucial source for generating successful decadal predictions of the KE variability.

As for the significant long-lead forecast skill detected in the seasonal prediction system (Fig. 7), we note a similarity between the behavior of the skillful prediction and the reemergence mechanism (Namias and Born 1970; Alexander and Deser 1995; Alexander et al. 1999), where the seasonal evolution of the mixed layer influences the behavior of surface fluxes. The reemergence mechanism is known to occur over large portions of the North Pacific Ocean, including the WBC system (Kwon et al. 2010). Supporting the previous view, we confirm that the reemergence mechanism at the KE region is detected in the SPEAR seasonal prediction system (Fig. 12). Specifically, a lag correlation map between the January KE index and ocean temperature anomalies shows that the surface anomalies formed over the deep mixed layer in the prior winter are sequestered in the summer, then gradually return to the surface in the following autumn. In the reemergence mechanism, the remaining subsurface ocean heat content can affect not only SST but also other oceanic parameters, such as a mixed layer formation and structure, buoyancy, and surface heat fluxes (Kwon et al. 2010; Na et al. 2018), affecting the seasonal prediction of KE SSH. This mechanism supports our results that the most skillful forecast initialized in winter and the best forecast for the fall (Fig. 7). The significant prediction skill of August KE SSH, however, is not clearly explained by the temperature anomalies in the mixed layer (Fig. 12) and needs to be further examined. In addition, in the reemergence mechanism, the temperature anomalies in the deep winter mixed layer are difficult to alter, whereas those in the shallow summer mixed layer tend to undergo a considerable change; thus, the shallowest mixed

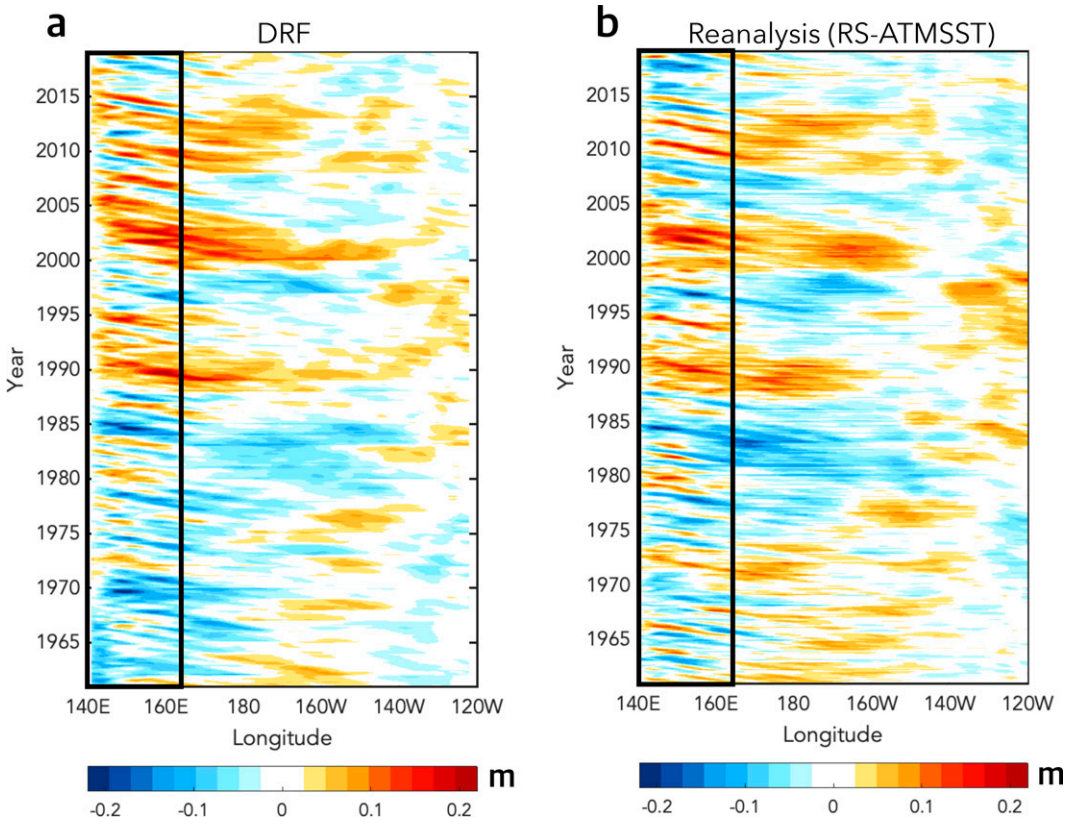

FIG. 11. Time–longitude plots of monthly SSH anomalies averaged between 31° and 38°N for (a) DRF with 1-yr lead and (b) RS-ATMSST. The period of 1961–2018 is shown. The black boxes correspond to the KE region.

layer in summer may amplify the forcing of zonal wind stress errors. Given that the seasonal changes in the reemergence mechanism are associated with the initialization month dependence in KE seasonal prediction skill, we may explain why the lowest and highest long-lead forecast skill come from forecasts initialized in summer and winter, respectively (Fig. 7a).

Based upon the above findings that the forecast skill varies seasonally, peaking for forecasts initialized in winter and verifying in fall, a comparison of September KE prediction skill from between decadal and seasonal forecasts initialized in January is shown in Fig. 13. The forecasts of the September KE SSH of DRF and SRF are both highly comparable with the observed September KE index from the observation satellite for the recent 30 years. A notable difference in the prediction performance between the two forecast systems is not observed.

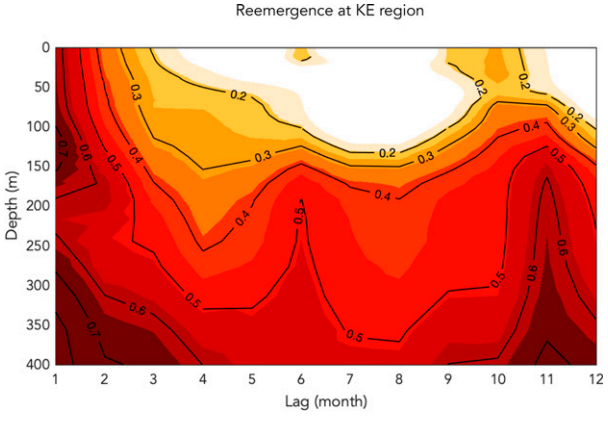

FIG. 12. Distribution of lag correlation coefficients for January KE index to the temperature anomalies from the surface to 400-m depth at the KE region (140°–165°E, 31°–38°N) for 1-month lead forecasts (SRF).

4. Summary and discussion

We use recently developed GFDL SPEAR reanalysis and forecast systems and show that the characteristics of decadal KE variability are reasonably represented and predicted in the current coupled climate models. A comparison of the KE spatiotemporal features reproduced in two reanalyses using different approaches (i.e., RS-ATMSST vs ODA) reveals that the assimilation of subsurface observations is critical to represent the latitudinal position and spatial structure of the KE oceanic front. Without constrained subsurface observations, the narrow frontal structure and the related oceanic variability of the KE system appear to be inadequately represented due

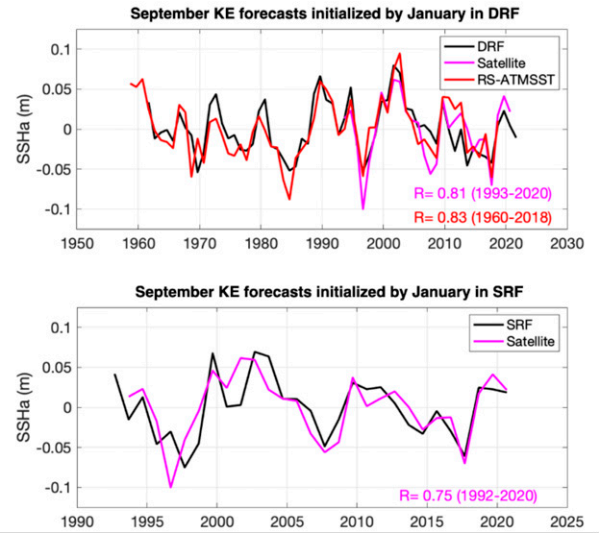

FIG. 13. A comparison of forecasts of September KE SSH initialized in January between the (top) decadal and (bottom) seasonal prediction. Correlations of the annual September KE index from between DRF and satellite (pink) or RS-ATMSST (red) are shown in the bottom right at the top panel. Correlations of the annual September KE index from between SRF and satellite (pink) are shown in the bottom right at the bottom panel.

to the intensification of KE jet overshoot, given 1° horizontal resolution of the ocean model used in this study. Our findings show that an important source of seasonal and decadal predictability of the KE system is the SSH variability associated with subsurface ocean variability that is driven by atmospheric forcing. The North Pacific atmospheric forcing [e.g., the North Pacific Oscillation (NPO)] is found to be the effectual source of the atmospheric-driven oceanic variability propagation to the KE region. Strong wind anomalies, particularly during the winter season, maximize the forecast skill as a favorable initial condition for KE prediction. Specifically, the larger amplitude of NPO during winters excites more deterministic remote forcing associated with wind-induced westward propagating Rossby waves. We confirm that decadal KE predictions provide considerable skill for lead times up to 5 years under January initializations. In addition, stronger basin-scale atmospheric forcing drives larger amplitude SSH anomalies through local Ekman transport and generates winter-to-winter persistence leading to long-lead forecast (4–12 months). We suggest that the long-lead skill of the seasonal KE prediction, which is mostly confined to winter initializations and forecasts of fall, is associated with the reemergence of subsurface ocean temperature fluxes where the mixed layer deepens in winter and shoals in spring. Through the analysis shown in this paper, we confirm that SPEAR seasonal and decadal prediction systems capture known mechanisms and critical processes governing the KE SSH changes and provide skillful KE predictions on both seasonal and decadal time scales.

For confident KE forecasts, dynamical model predictions are crucial because previous simple prediction models (i.e., linear Rossby wave equation) are limited by an inability to detect full dynamics of air–sea coupled processes and physical segments of the KE system. For example, Qiu et al. (2020) noted a recent sudden transition of the KE state from a negative to a positive phase, which was not predicted in their previous KE forecast (Qiu et al. 2014). Specifically, the study shows that the KE state (after 2014), which was predicted to be in a negative phase up until about 2019, abruptly transitioned to a positive state in late 2017. The study attributes the failure of their KE forecasts to unexpected large meanders that occurred in the Kuroshio region to the south of Japan in early 2017, where the meander can be highly irregular and chaotic with no dominant periodicities nor a preferred duration (Qiu and Miao 2000; Usui et al. 2013). The study points out that while over the past three decades the wind-forced KE variability prevails on the decadal time scale, the recent large meander observed in the Kuroshio in 2017, which was an unforeseen rare episode, has unexpectedly triggered positive KE SSH anomalies. This episode resets the KE state as negative-to-positive SSH change, as shown in Figs. 14a and 14b. The study has demonstrated that the meander-induced KE change is found to be significant because it affects the overlying storm track and North Pacific atmospheric circulations (i.e., wind pattern) as substantially as wind-induced decadal KE changes.

Using SPEAR dynamical model KE forecasts, we find that we were able to detect the recent transition of the KE decadal state as shown in Figs. 14c and 14d. At first glance, the decadal KE forecasts initialized in 2015 (camouflage color in Fig. 14c) and 2016 (green in Fig. 14c) predict the continuous neutral KE phase for all of 2017, which seemingly fails to capture the negative KE phase in 2017. However, as shown in the observation satellite, the forecasts initialized in 2016 (green in Fig. 14c) and 2017 (blue in Fig. 14c) exhibit a transition to a positive KE state after late 2017 and successfully predict the continuous positive KE after 2018. The seasonal KE forecasts initialized in late 2016 (green in Fig. 14d) and early 2017 (blue in Fig. 14c) also successfully detect the transitioned KE index after late 2017. Both decadal and seasonal KE forecasts consistently indicate above-average KE SSH anomalies for the next few years (i.e., 2021 and 2022). In relation to what Qiu et al. (2020) have reported, these results imply that the dynamical model forecasts, especially SRF where the subsurface ocean is constrained by observations, may have the capability of capturing the impact of the Kuroshio path associated with large meanders as well as the delayed oceanic adjustment (Fig. S2). Supporting this, Qiu and Chen (2021) revisit the occurrence of the large meander south of Japan in 2017 and conclude that such meanders might not be an entirely intrinsic process but may be partly connected to large-scale variability (e.g., regional wind forcing during a positive phase of the PDO). Our results imply that the SPEAR prediction system can anticipate some Kuroshio meanders that are driven by large-scale wind forcing, but may still struggle to resolve the random, internally generated component of meander activity.

Given the effective initialization strategy (e.g., winter initial condition), SPEAR forecasts provide a near-term prediction

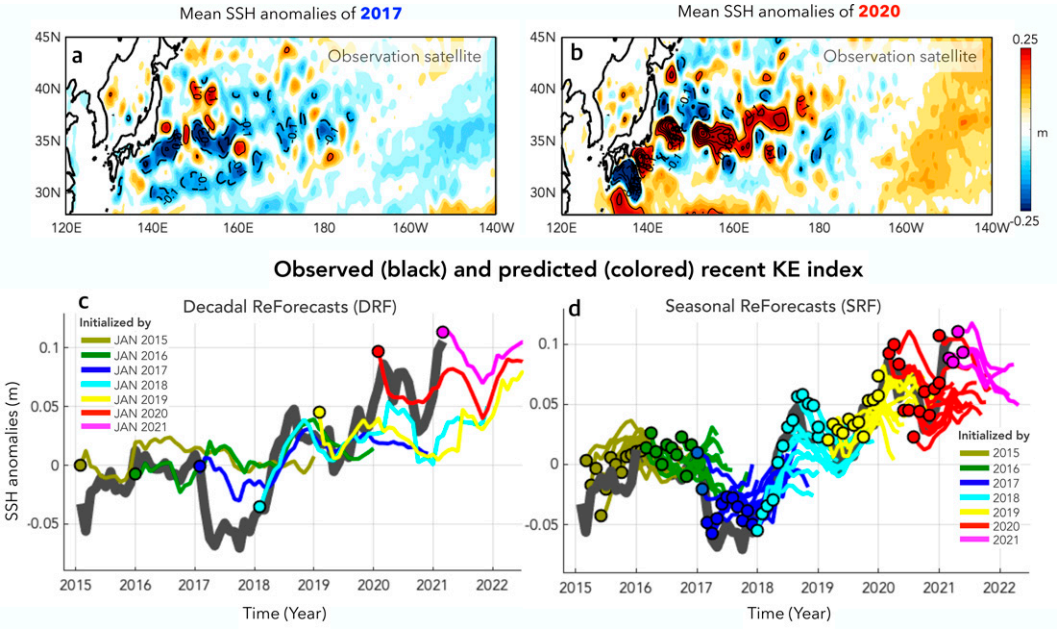

FIG. 14. Recent transition of the KE phase and KE forecast for 2022/23. Observed annual mean SSH anomalies over the KE region in (a) 2017 (negative phase of KE) and (b) 2020 (positive phase of KE). (c),(d) Detections of the KE phase transition during 2015–21 in SRF. The monthly KE index from observation satellite (black) and DRF (colors; ensemble mean) with forecast lead times of 1–48 months is shown in (c). The monthly KE index from observation satellite (black) and SRF (colors, ensemble mean) with forecast lead time of 1–12 months is shown in (d). The circles denote initialization months.

skill of the KE above persistence for more than a couple of years in advance, which is highly comparable to the observation from satellite altimetry (Figs. 4a and 6d). Under the limited computational resources, the current initialization procedure, where the current decadal prediction system is based on only atmospheric/SST restoring, could be an efficient way to resolve wind-driven low-frequency KE variability, which is mainly reliable to the given initialized atmospheric anomalies. The short-term KE forecast, on the other hand, highly requires nonlinear ocean dynamics, so the current initialization configuration, including atmospheric restoring and ocean data assimilation, also would be adequate.

Importantly, the ability to predict decadal variations of KE SSH anomalies provides opportunities to project the regional climate, such as the decadal behavior of the tropical rainfall (Fig. 15). As Joh et al. (2021) have confirmed through complementary analysis using observations and numerical and empirical dynamical models, the KE may exert a persistent downstream response (i.e., wind stress curl) that projects on atmospheric forcing of Pacific meridional modes and central Pacific ENSO, especially for the recent period. Consistent with this previous finding, we find that the decadal KE SSH changes lead the tropical precipitation anomalies (i.e., in the Niño-3.4 region, 5°S–5°N, 120°–170°W) by 2.5 years. The correlations are statistically significant for the whole period (for 1960–2019, $R = 0.49$, significant at $p < 0.05$), and exceptionally high for recent decades (for 1985–2019, significant $R = 0.73$ at $p < 0.01$) in the SPEAR reanalysis system (Fig. 14b). A strong overlapping of the decadal fluctuations between the KE SSH and tropical precipitation in the east-central Pacific (Niño-3.4 region) suggests that the KE forecast may act as a potential source for multiyear predictability for tropical variability, such as ENSO.

While the ocean–atmosphere coupling is important to long-term KE prediction as demonstrated in Qiu et al. (2014), due to insufficient horizontal resolution of the SPEAR ocean model, the contribution of the atmospheric response to the decadal KE state in the present study is considered insignificant. In other words, the coupled atmospheric response may not be the crucial source of skill in the current SPEAR prediction system. However, we believe that increasing ocean model resolution is beneficial not only for the long-term KE prediction but also for the short-term forecast because of the improved contributions of short-lived intrinsic mesoscale eddy activity for resolving dynamic properties of the KE system and the impact on the large-scale atmospheric variability. Upcoming high-resolution (0.25° for ocean/atmospheric models) SPEAR coupled systems (SPEAR_HI_25) may facilitate extensive investigation of detailed physical characteristics of the KE region, including the volume transport, high mesoscale eddy variability, baroclinic instability, and so on. Increases in model resolution may improve the representation of ocean dynamics in the western boundary current system by more accurately capturing oceanic fronts (i.e., sea surface gradient) and small-scale intrinsic ocean dynamics. We expect that enhanced

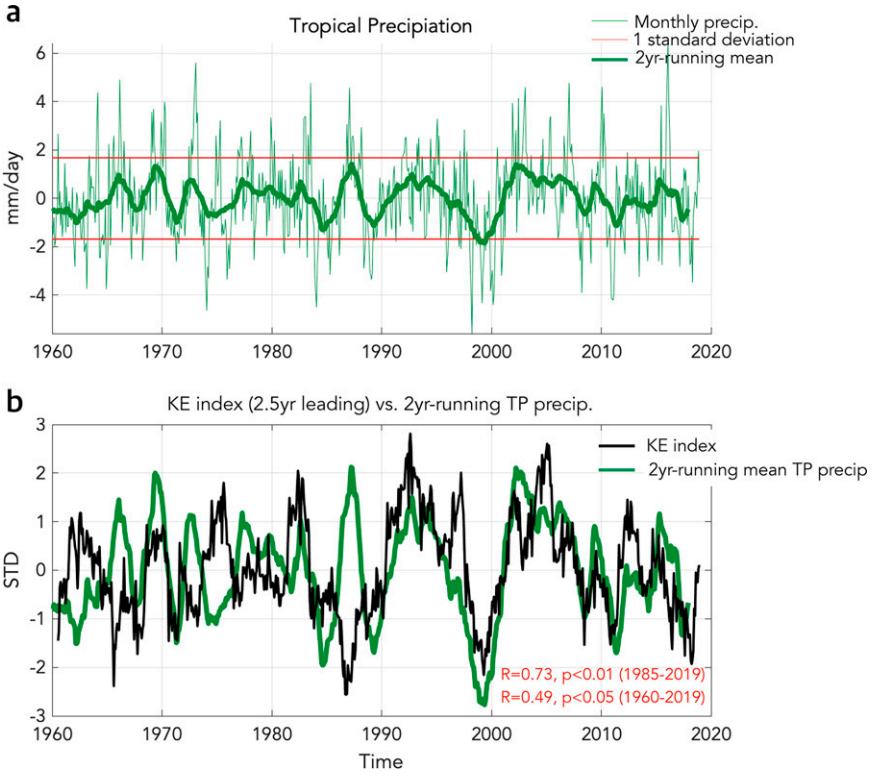

FIG. 15. Impact of KE decadal variability on tropical precipitation. (a) Time series of monthly precipitation anomalies (thin green line), its one standard deviation (red line), and 2-yr running mean precipitation (bold green line) for the Niño-3.4 region (5°S–5°N, 120°–170°W). (b) A comparison of 2-yr running mean tropical precipitation (bold green line) and KE index (bold black line), where the KE leads by 2.5 years. Correlations between the KE and tropical precipitation are shown at the bottom right.

air–sea coupling and more realistic atmospheric response along the front (i.e., extratropical storm track) will allow the detection of the deterministic KE atmospheric/oceanic feedback onto large-scale air–sea interactions and climate variability.

Acknowledgments. The authors are grateful to Dr. Kai-Chih Tseng and Dr. Matthew Harrison for constructive reviews on the earlier version of this manuscript and three anonymous reviewers for comments that helped to significantly improve the manuscript. The NCEP–NCAR reanalysis data used in this study were obtained from https://psl.noaa.gov/data/gridded/data.ncep.reanalysis.html. The merged satellite altimeter data of the Copernicus Marine and Environment Monitoring Service was from https://marine.copernicus.eu/. We acknowledge the Cooperative Institute for Modeling the Earth System (CIMES) program, a collaboration between Princeton University and the NOAA Geophysical Fluid Dynamics Laboratory. The study was prepared by Youngji Joh under Award NA18OAR4320123 from the National Oceanic and Atmospheric Administration, U.S. Department of Commerce. The statements, findings, conclusions, and recommendations are those of the author(s) and do not necessarily reflect the views of the National Oceanic and Atmospheric Administration, or the U.S. Department of Commerce.

Data availability statement. The SPEAR predictions analyzed in this study are partially available through the FTP link ftp://data1.gfdl.noaa.gov/users/youngji.joh/kuroshio_extension/GFDL-SPEAR/. Further information about the data used in this study and conditions for access are available upon request.

REFERENCES

Adcroft, A., and Coauthors, 2019: The GFDL global ocean and sea ice model OM4.0: Model description and simulation features. *J. Adv. Model. Earth Syst.*, **11**, 3167–3211, https://doi.org/10.1029/2019MS001726.

Alexander, M. A., and C. Deser, 1995: A mechanism for the recurrence of wintertime midlatitude SST anomalies. *J. Oceanogr.*, **25**, 122–137, https://doi.org/10.1175/1520-0485(1995)025<0122:AMFTRO>2.0.CO;2.

——, and J. D. Scott, 2008: The role of Ekman ocean heat transport in the Northern Hemisphere response to ENSO. *J. Climate*, **21**, 5688–5707, https://doi.org/10.1175/2008JCLI2382.1.

——, C. Deser, and M. S. Timlin, 1999: The reemergence of SST anomalies in the North Pacific Ocean. *J. Climate*, **12**, 2419–2433, https://doi.org/10.1175/1520-0442(1999)012<2419:TROSAI>2.0.CO;2.

——, I. Bladé, M. Newman, J. R. Lanzante, N.-C. Lau, and J. D. Scott, 2002: The atmospheric bridge: The influence of ENSO teleconnections on air–sea interaction over the global oceans. *J. Climate*, **15**, 2205–2231, https://doi.org/10.1175/1520-0442(2002)015<2205:TABTIO>2.0.CO;2.

Anderson, B. T., 2019: Empirical evidence linking the Pacific decadal precession to Kuroshio Extension variability. *J. Geophys. Res. Atmos.*, **124**, 12 845–12 863, https://doi.org/10.1029/2019JD031163.

Argo, 2019: Argo float data and metadata from Global Data Assembly Centre (Argo GDAC). SEANOE, accessed 2019, https://doi.org/10.17882/42182.

Ceballos, L. I., E. Di Lorenzo, C. D. Hoyos, N. Schneider, and B. Taguchi, 2009: North Pacific Gyre Oscillation synchronizes climate fluctuations in the eastern and western boundary systems. *J. Climate*, **22**, 5163–5174, https://doi.org/10.1175/2009JCLI2848.1.

Delworth, T. L., and Coauthors, 2020: SPEAR: The next generation GFDL modeling system for seasonal to multidecadal prediction and projection. *J. Adv. Model. Earth Syst.*, **12**, e2019MS001895, https://doi.org/10.1029/2019MS001895.

Deser, C., M. A. Alexander, and M. S. Timlin, 1999: Evidence for a wind-driven intensification of the Kuroshio Current Extension from the 1970s to the 1980s. *J. Climate*, **12**, 1697–1706, https://doi.org/10.1175/1520-0442(1999)012<1697:EFAWDI>2.0.CO;2.

——, ——, and ——, 2003: Understanding the persistence of sea surface temperature anomalies in midlatitudes. *J. Climate*, **16**, 57–72, https://doi.org/10.1175/1520-0442(2003)016<0057:UTPOSS>2.0.CO;2.

Fedele, G., A. Bellucci, S. Masina, and S. Pierini, 2021: Decadal variability of the Kuroshio Extension: The response of the jet to increased atmospheric resolution in a coupled ocean–atmosphere model. *Climate Dyn.*, **56**, 1227–1249, https://doi.org/10.1007/s00382-020-05528-4.

Frankignoul, C., and E. Kestenare, 2002: The surface heat flux feedback. Part I: Estimates from observations in the Atlantic and the North Pacific. *Climate Dyn.*, **19**, 633–647, https://doi.org/10.1007/s00382-002-0252-x.

——, P. Müller, and E. Zorita, 1997: A simple model of the decadal response of the ocean to stochastic wind forcing. *J. Phys. Oceanogr.*, **27**, 1533–1546, https://doi.org/10.1175/1520-0485(1997)027<1533:ASMOTD>2.0.CO;2.

Hamill, T. M., 2001: Interpretation of rank histograms for verifying ensemble forecasts. *Mon. Wea. Rev.*, **129**, 550–560, https://doi.org/10.1175/1520-0493(2001)129<0550:IORHFV>2.0.CO;2.

Huang, B., and Coauthors, 2017: Extended Reconstructed Sea Surface Temperature, version 5 (ERSSTv5): Upgrades, validations, and intercomparisons. *J. Climate*, **30**, 8179–8205, https://doi.org/10.1175/JCLI-D-16-0836.1.

Jacox, M. G., M. A. Alexander, C. A. Stock, and G. Hervieux, 2019: On the skill of seasonal sea surface temperature forecasts in the California Current System and its connection to ENSO variability. *Climate Dyn.*, **53**, 7519–7533, https://doi.org/10.1007/s00382-017-3608-y.

Joh, Y., and E. Di Lorenzo, 2019: Interactions between Kuroshio Extension and central tropical Pacific lead to preferred decadal-timescale oscillations in Pacific climate. *Sci. Rep.*, **9**, 13558, https://doi.org/10.1038/s41598-019-49927-y.

——, ——, L. Siqueira, and B. P. Kirtman, 2021: Enhanced interactions of Kuroshio Extension with tropical Pacific in a changing climate. *Sci. Rep.*, **11**, 6247, https://doi.org/10.1038/s41598-021-85582-y.

Kalnay, E., and Coauthors, 1996: The NCEP/NCAR 40-Year Reanalysis Project. *Bull. Amer. Meteor. Soc.*, **77**, 437–471, https://doi.org/10.1175/1520-0477(1996)077<0437:TNYRP>2.0.CO;2.

Kelly, K. A., and B. Qiu, 1995: Heat flux estimates for the western North Atlantic. Part II: The upper-ocean heat budget. *J. Phys. Oceanogr.*, **25**, 2361–2373, https://doi.org/10.1175/1520-0485(1995)025<2361:HFEFTW>2.0.CO;2.

——, and S. Dong, 2004: The relationship of western boundary current heat transport and storage to mid-latitude ocean–atmosphere interaction. *J. Climate*, **17**, 573–588, https://doi.org/10.1029/147GM19.

——, R. J. Small, R. M. Samelson, B. Qiu, T. M. Joyce, Y.-O. Kwon, and M. F. Cronin, 2010: Western boundary currents and frontal air–sea interaction: Gulf Stream and Kuroshio Extension. *J. Climate*, **23**, 5644–5667, https://doi.org/10.1175/2010JCLI3346.1.

Kharin, V. V., G. J. Boer, W. J. Merryfield, J. F. Scinocca, and W. S. Lee, 2012: Statistical adjustment of decadal predictions in a changing climate. *Geophys. Res. Lett.*, **39**, L19705, https://doi.org/10.1029/2012GL052647.

Knaff, J. A., and C. W. Landsea, 1997: An El Niño–Southern Oscillation climatology and persistence (CLIPER) forecasting scheme. *Wea. Forecasting*, **12**, 633–652, https://doi.org/10.1175/1520-0434(1997)012<0633:AENOSO>2.0.CO;2.

Kobayashi, S., and Coauthors, 2015: The JRA-55 reanalysis: General specifications and basic characteristics. *J. Meteor. Soc. Japan. II*, **93**, 5–48, https://doi.org/10.2151/jmsj.2015-001.

Kwon, Y.-O., and C. Deser, 2007: North Pacific decadal variability in the Community Climate System Model version 2. *J. Climate*, **20**, 2416–2433, https://doi.org/10.1175/JCLI4103.1.

——, M. A. Alexander, N. A. Bond, C. Frankignoul, H. Nakamura, B. Qiu, and L. A. Thompson, 2010: Role of the Gulf Stream and Kuroshio–Oyashio systems in large-scale atmosphere–ocean interaction: A review. *J. Climate*, **23**, 3249–3281, https://doi.org/10.1175/2010JCLI3343.1.

Landerer, F. W., P. J. Gleckler, and T. Lee, 2014: Evaluation of CMIP5 dynamic sea surface height multi-model simulations against satellite observations. *Climate Dyn.*, **43**, 1271–1283, https://doi.org/10.1007/s00382-013-1939-x.

Latif, M., and T. P. Barnett, 1994: Causes of decadal climate variability over the North Pacific and North America. *Science*, **266**, 634–637, https://doi.org/10.1126/science.266.5185.634.

——, and ——, 1996: Decadal climate variability over the North Pacific and North America. *J. Climate*, **9**, 2407–2423, https://doi.org/10.1175/1520-0442(1996)009<2407:DCVOTN>2.0.CO;2.

Lee, T., D. E. Waliser, J.-L. F. Li, F. W. Landerer, and M. M. Gierach, 2013: Evaluation of CMIP3 and CMIP5 wind stress climatology using satellite measurements and atmospheric reanalysis products. *J. Climate*, **26**, 5810–5826, https://doi.org/10.1175/JCLI-D-12-00591.1.

Linkin, M. E., and S. Nigam, 2008: The North Pacific Oscillation–west Pacific teleconnection pattern: Mature-phase structure and winter impacts. *J. Climate*, **21**, 1979–1997, https://doi.org/10.1175/2007JCLI2048.1.

Liu, Z., and M. Alexander, 2007: Atmospheric bridge, oceanic tunnel, and global climatic teleconnections. *Rev. Geophys.*, **45**, RG2005, https://doi.org/10.1029/2005RG000172.

Lu, F., and Coauthors, 2020: GFDL's SPEAR seasonal prediction system: Initialization and Ocean Tendency Adjustment (OTA) for coupled model predictions. *J. Adv. Model. Earth Syst.*, **12**, e2020MS002149, https://doi.org/10.1029/2020MS002149.

Ma, X., and Coauthors, 2015: Distant influence of Kuroshio eddies on North Pacific weather patterns? *Sci. Rep.*, **5**, 17785, https://doi.org/10.1038/srep17785.

——, P. Chang, R. Saravanan, R. Montuoro, H. Nakamura, D. Wu, X. Lin, and L. Wu, 2017: Importance of resolving Kuroshio front and eddy influence in simulating the North Pacific storm track. *J. Climate*, **30**, 1861–1880, https://doi.org/10.1175/JCLI-D-16-0154.1.

Meehl, G. A., and Coauthors, 2014: Decadal climate prediction: An update from the trenches. *Bull. Amer. Meteor. Soc.*, **95**, 243–267, https://doi.org/10.1175/BAMS-D-12-00241.1.

Miller, A. J., D. R. Cayan, and W. B. White, 1998: A westward-intensified decadal change in the North Pacific thermocline and gyre-scale circulation. *J. Climate*, **11**, 3112–3127, https://doi.org/10.1175/1520-0442(1998)011<3112:AWIDCI>2.0.CO;2.

Morioka, Y., S. Varlamov, and Y. Miyazawa, 2019: Role of Kuroshio current in fish resource variability off southwest Japan. *Sci. Rep.*, **9**, 17942, https://doi.org/10.1038/s41598-019-54432-3.

Na, H., K.-Y. Kim, S. Minobe, and Y. N. Sasaki, 2018: Interannual to decadal variability of the upper-ocean heat content in the western North Pacific and its relationship to oceanic and atmospheric variability. *J. Climate*, **31**, 5107–5125, https://doi.org/10.1175/JCLI-D-17-0506.1.

Nakamura, H., G. Lin, and T. Yamagata, 1997: Decadal climate variability in the North Pacific during the recent decades. *Bull. Amer. Meteor. Soc.*, **78**, 2215–2225, https://doi.org/10.1175/1520-0477(1997)078<2215:DCVITN>2.0.CO;2.

Namias, J., and R. M. Born, 1970: Temporal coherence in North Pacific sea surface temperature patterns. *J. Geophys. Res.*, **75**, 5952–5955, https://doi.org/10.1029/JC075i030p05952.

Nonaka, M., and S.-P. Xie, 2000: Propagation of North Pacific interdecadal subsurface temperature anomalies in an ocean GCM. *Geophys. Res. Lett.*, **27**, 3747–3750, https://doi.org/10.1029/2000GL011488.

——, Y. Sasai, H. Sasaki, B. Taguchi, and H. Nakamura, 2016: How potentially predictable are midlatitude ocean currents? *Sci. Rep.*, **6**, 20153, https://doi.org/10.1038/srep20153.

Panofsky, H. A., and G. W. Brier, 1958: *Some Applications of Statistics to Meteorology*. The Pennsylvania State University, 224 pp.

Park, S., C. Deser, and M. A. Alexander, 2005: Estimation of the surface heat flux response to sea surface temperature anomalies over the global oceans. *J. Climate*, **18**, 4582–4599, https://doi.org/10.1175/JCLI3521.1.

Piazza, M., L. Terray, J. Boé, E. Maisonnave, and E. Sanchez-Gomez, 2016: Influence of small-scale North Atlantic sea surface temperature patterns on the marine boundary layer and free troposphere: A study using the atmospheric ARPEGE model. *Climate Dyn.*, **46**, 1699–1717, https://doi.org/10.1007/s00382-015-2669-z.

Pierce, D. W., T. P. Barnett, N. Schneider, R. Saravanan, D. Dommenget, and M. Latif, 2001: The role of ocean dynamics in producing decadal climate variability in the North Pacific. *Climate Dyn.*, **18**, 51–70, https://doi.org/10.1007/s003820100158.

Qiu, B., 2000: Interannual variability of the Kuroshio Extension System and its impact on the wintertime SST field. *J. Phys. Oceanogr.*, **30**, 1486–1502, https://doi.org/10.1175/1520-0485(2000)030<1486:IVOTKE>2.0.CO;2.

——, 2002: Large-scale variability in the midlatitude subtropical and subpolar North Pacific Ocean: Observations and causes. *J. Phys. Oceanogr.*, **32**, 353–375, https://doi.org/10.1175/1520-0485(2002)032<0353:LSVITM>2.0.CO;2.

——, 2003: Kuroshio Extension variability and forcing of the Pacific decadal oscillations: Responses and potential feedback. *J. Phys. Oceanogr.*, **33**, 2465–2482, https://doi.org/10.1175/2459.1.

——, and K. A. Kelly, 1993: Upper-ocean heat balance in the Kuroshio Extension region. *J. Phys. Oceanogr.*, **23**, 2027–2041, https://doi.org/10.1175/1520-0485(1993)023<2027:UOHBIT>2.0.CO;2.

——, and W. Miao, 2000: Kuroshio path variations south of Japan: Bimodality as a self-sustained internal oscillation. *J. Phys. Oceanogr.*, **30**, 2124–2137, https://doi.org/10.1175/1520-0485(2000)030<2124:KPVSOJ>2.0.CO;2.

——, and S. Chen, 2005: Variability of the Kuroshio Extension jet, recirculation gyre, and mesoscale eddies on decadal time scales. *J. Phys. Oceanogr.*, **35**, 2090–2103, https://doi.org/10.1175/JPO2807.1.

——, and ——, 2010: Eddy-mean flow interaction in the decadally modulating Kuroshio Extension System. *Deep-Sea Res. II*, **57**, 1098–1110, https://doi.org/10.1016/j.dsr2.2008.11.036.

——, and ——, 2021: Revisit of the occurrence of the Kuroshio large meander South of Japan. *J. Phys. Oceanogr.*, **51**, 3679–3694, https://doi.org/10.1175/JPO-D-21-0167.1.

——, N. Schneider, and S. Chen, 2007: Coupled decadal variability in the North Pacific: An observationally constrained idealized model. *J. Climate*, **20**, 3602–3620, https://doi.org/10.1175/JCLI4190.1.

——, S. Chen, N. Schneider, and B. Taguchi, 2014: A coupled decadal prediction of the dynamic state of the Kuroshio Extension System. *J. Climate*, **27**, 1751–1764, https://doi.org/10.1175/JCLI-D-13-00318.1.

——, ——, ——, E. Oka, and S. Sugimoto, 2020: On the reset of the wind-forced decadal Kuroshio Extension variability in late 2017. *J. Climate*, **33**, 10 813–10 828, https://doi,org/10.1175/jcli-d-20-0237.1

Reynolds, R. W., N. A. Rayner, T. M. Smith, D. C. Stokes, and W. Wang, 2002. An improved in situ and satellite SST analysis for climate. *J. Climate*, **15**, 1609–1625, https://doi.org/10.1175/1520-0442(2002)015<1609:AIISAS>2.0.CO;2.

——, T. M. Smith, C. Liu, D. B. Chelton, K. S. Casey, and M. G. Schlax, 2007: Daily high-resolution-blended analyses for sea surface temperature. *J. Climate*, **20**, 5473–5496, https://doi.org/10.1175/2007JCLI1824.1.

Rogers, J. C., 1981: The North-Pacific Oscillation. *J. Climatol.*, **1**, 39–57, https://doi.org/10.1002/joc.3370010106.

Saha, S., and Coauthors, 2010: The NCEP Climate Forecast System Reanalysis. *Bull. Amer. Meteor. Soc.*, **91**, 1015–1057, https://doi.org/10.1175/2010BAMS3001.1

Sasaki, Y. N., S. Minobe, and N. Schneider, 2013: Decadal response of the Kuroshio Extension jet to Rossby waves: Observation and thin-jet theory. *J. Phys. Oceanogr.*, **43**, 442–456, https://doi.org/10.1175/JPO-D-12-096.1.

Schneider, N., and A. J. Miller, 2001: Predicting western North Pacific Ocean climate. *J. Climate*, **14**, 3997–4002, https://doi.org/10.1175/1520-0442(2001)014<3997:PWNPOC>2.0.CO;2.

——, and B. D. Cornuelle, 2005: The forcing of the Pacific decadal oscillation. *J. Climate*, **18**, 4355–4373, https://doi.org/10.1175/JCLI3527.1.

——, A. J. Miller, and D. W. Pierce, 2002: Anatomy of North Pacific decadal variability. *J. Climate*, **15**, 586–605, https://doi.org/10.1175/1520-0442(2002)015<0586:AONPDV>2.0.CO;2.

Seager, R., Y. Kushnir, N. H. Naik, M. A. Cane, and J. Miller, 2001: Wind-driven shifts in the latitude of the Kuroshio–Oyashio Extension and generation of SST anomalies on decadal timescales. *J. Climate*, **14**, 4249–4265, https://doi.org/10.1175/1520-0442(2001)014<4249:WDSITL>2.0.CO;2.

Siqueira, L., B. P. Kirtman, and L. C. Laurindo, 2021: Forecasting remote atmospheric responses to decadal Kuroshio stability transitions. *J. Climate*, **34**, 379–395, https://doi.org/10.1175/JCLI-D-20-0139.1.

Stock, C. A., and Coauthors, 2015: Seasonal sea surface temperature anomaly prediction for coastal ecosystems. *Prog. Oceanogr.*, **137**, 219–236, https://doi.org/10.1016/j.pocean.2015.06.007.

Sun, C., and Coauthors, 2010: The data management system for the global temperature and salinity profile program. *Proc. OceanObs'09: Sustained Ocean Observation and Information for Society*, Venice, Italy, ESA Publication WPP-306, https://doi.org/10.5270/OceanObs09.cwp.86.

Sutton, R., and P. P. Mathieu, 2002: Response of the atmosphere–ocean mixed-layer system to anomalous ocean heat-flux convergence. *Quart. J. Roy. Meteor. Soc.*, **128**, 1259–1275, https://doi.org/10.1256/003590002320373283.

Taguchi, B., and N. Schneider, 2014: Origin of decadal-scale, eastward-propagating heat content anomalies in the North Pacific. *J. Climate*, **27**, 7568–7586, https://doi.org/10.1175/JCLI-D-13-00102.1.

——, S.-P. Xie, N. Schneider, M. Nonaka, H. Sasaki, and Y. Sasai, 2007: Decadal variability of the Kuroshio Extension: Observations and an eddy-resolving model hindcast. *J. Climate*, **20**, 2357–2377, https://doi.org/10.1175/JCLI4142.1.

——, B. Qiu, M. Nonaka, H. Sasaki, S.-P. Xie, and N. Schneider, 2010: Decadal variability of the Kuroshio Extension: Mesoscale eddies and recirculations. *Ocean Dyn.*, **60**, 673–691, https://doi.org/10.1007/s10236-010-0295-1.

Trenberth, K. E., and J. W. Hurrell, 1994: Decadal atmosphere–ocean variations in the Pacific. *Climate Dyn.*, **9**, 303–319, https://doi.org/10.1007/BF00204745.

——, G. W. Branstator, D. Karoly, A. Kumar, N.-C. Lau, and C. Ropelewski, 1998: Progress during TOGA in understanding and modeling global teleconnections associated with tropical sea surface temperatures. *J. Geophys. Res.*, **103**, 14 291–14 324, https://doi.org/10.1029/97JC01444.

Usui, N., H. Tsujino, H. Nakano, and S. Matsumoto, 2013: Long-term variability of the Kuroshio path south of Japan. *J. Oceanogr.*, **69**, 647–670, https://doi.org/10.1007/s10872-013-0197-1.

Walker, G. T., and E. W. Bliss, 1932: World weather V. *Mem. Roy. Meteor. Soc.*, **4**, 53–84.

Yang, X., and Coauthors, 2013: A predictable AMO-like pattern in the GFDL fully coupled ensemble initialization and decadal forecasting system. *J. Climate*, **26**, 650–661, https://doi.org/10.1175/JCLI-D-12-00231.1.

——, L. Jia, S. B. Kapnick, T. L. Delworth, G. A. Vecchi, R. Gudgel, S. Underwood, and F. Zeng, 2018: On the seasonal prediction of the western United States El Niño precipitation pattern during the 2015/16 winter. *Climate Dyn.*, **51**, 3765–3783, https://doi.org/10.1007/s00382-018-4109-3.

——, and Coauthors, 2021: On the development of GFDL's decadal prediction system: Initialization approaches and retrospective forecast assessment. *J. Adv. Model. Earth Syst.*, **13**, e2021MS002529, https://doi.org/10.1029/2021MS002529.

Zhao, M., and Coauthors, 2018a: The GFDL Global Atmosphere and Land Model AM4.0/LM4.0: 1. Simulation characteristics with prescribed SSTs. *J. Adv. Model. Earth Syst.*, **10**, 691–734, https://doi.org/10.1002/2017MS001208.

——, and Coauthors, 2018b: The GFDL Global Atmosphere and Land Model AM4.0/LM4.0: 2. Model description, sensitivity studies, and tuning strategies. *J. Adv. Model. Earth Syst.*, **10**, 735–769, https://doi.org/10.1002/2017MS001209.

Zhou, G., M. Latif, R. J. Greatbatch, and W. Park, 2015: Atmospheric response to the North Pacific enabled by daily sea surface temperature variability. *Geophys. Res. Lett.*, **42**, 7732–7739, https://doi.org/10.1002/2015GL065356.